# Observing the forbidden zone for light

Simon R. Huisman

Master's Thesis
Applied Physics, University of Twente
January 2010

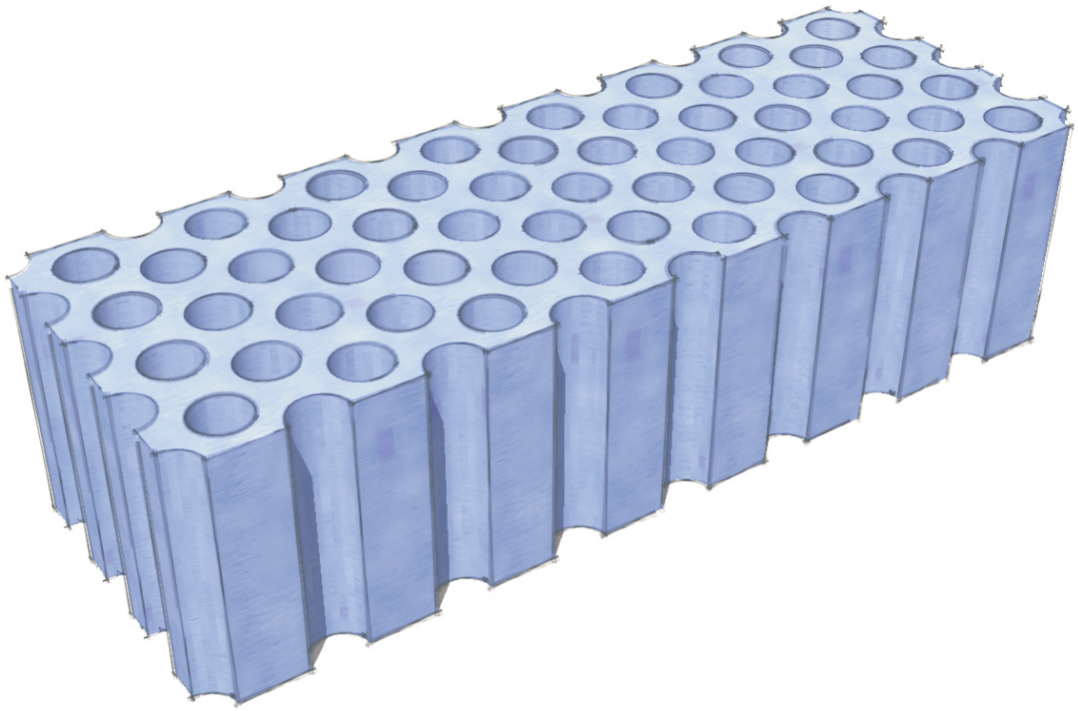

# Observing the forbidden zone for light

S.R. Huisman

Master's Thesis,
Applied Physics, University of Twente
March 2009 - January 2010

**Graduation committee:**
Dr. G.H.L.A. Brocks (CMS)
Ir. M.D. Leistikow (COPS and AMOLF)
Dr. R.V. Nair (COPS)
Prof. Dr. W.L. Vos (COPS and AMOLF)

**This work was done at:**
Photonic Bandgaps group
Center for Nanophotonics
FOM institute for Atomic and Molecular Physics (AMOLF)
Sciencepark 102
1098 XG Amsterdam

Complex Photonic Systems (COPS)
MESA+ Institute for Nanotechnology
Faculty of Science and Technology
University of Twente
P.O. Box 217
7500 AE Enschede

# Abstract

We experimentally study light propagation in novel two-dimensional and three-dimensional macroporous photonic crystals. These crystals strongly interact with light for near-infrared frequencies.

We present polarization resolved reflectivity from two-dimensional photonic crystals with a centred rectangular lattice. The reflectivity has been collected from the $\Gamma M'$- and $\Gamma K$-directions for crystals with a range of pore diameters. Stopgaps and a two-dimensional band gap for TE polarized light have been identified by comparing spectra with calculated photonic dispersion relations and Bragg conditions. In the $\Gamma K$-direction, a lowest frequency diffraction peak exists that cannot be explained with simple Bragg diffraction. Calculated dispersion relations indicate that multiple Bragg diffraction occurs on the (10) and (01) crystal planes, causing an experimentally observed distinction between a simple Bragg diffraction peak and a sub-Bragg diffraction peak.

Polarization resolved reflectivity spectra are presented for three-dimensional silicon inverse woodpile photonic crystals. The reflectivity has been collected from the $\Gamma X$- and $\Gamma Z$-directions for crystals with a range of pore diameters. Diffraction peaks are in reasonable agreement with calculated dispersion relations. Spectra demonstrate for several crystals overlapping diffraction peaks for different polarizations and directions, indicating the presence of a photonic band gap.

A two-dimensional photonic crystal was embedded in a lead sulphide quantum dot suspension to study the crystal's influence on spontaneous emission. Emission maxima have been observed near the high-frequency edge of the two-dimensional band gap for TE polarized light.

# Acknowledgements

In the past ten months I have studied the interaction between light and new types of photonic crystals. This exciting work has been done at the Photonic Bandgaps group (PBG) at the FOM Institute for Atomic and Molecular Physics (AMOLF) in Amsterdam and the Complex Photonic Systems (COPS) group, part of the MESA+ Institute for Nanotechnology at the University of Twente. Being a member of both ambitious groups has given me great insights. I enjoyed the discussions, attitude, support and working atmospheres in both groups.

I thank Willem Vos for giving me the possibility to work on this project. You have given me valuable insights in experimental optics and conducting research. I appreciate your critical attitude and your never-ending interest in new results. I would like to thank Merel Leistikow for daily supervision and guidance. I appreciate your support, our discussions, and keeping overview of the progress. Your enthusiasm in conducting experiments was of great inspiration. I thank Rajesh Nair for working together on the reflectivity measurements. I believe that our experiments, discussions and analysis have led to nice results. Thank you for being a member of my graduation committee.

The photonic crystals have been fabricated by Hannie van den Broek, Willem Tjerkstra and Léon Woldering. It has been a privilege to work with these crystals. Thank you for your advice and support. I would like to thank Cock Harteveld and Iwert Mijnders for technical support and organizing the move of PBG to COPS. I thank Allard Mosk for simulations, interesting discussions and for his role as study coordinator. I am grateful to Alex Hartsuiker and Bart Husken for discussions and developing the setups.

For inspiring discussions, education, support and good company I would like to thank all members of the Photonic Bandgaps, Photon Scattering and COPS groups; Ad, Bart, Bas, Bergin, Bernard, Danang, Duygu, Elbert, Emre, Frerik, Georgios, Hakki, Jochen, Karen, Marlon, Paolo, Patrick, Ramy, Rob, Sanli and Timmo. I would like to thank Geert Brocks of the Computational Materials Science group at the University of Twente for being a member of my graduation committee. I thank the members of the Center for Nanophotonics for stimulating discussions. I thank the members of TCO for the design and fabrication of the nice sample holder.

Finally, I would like to thank my family for advice, care, understanding, encouragement, and support.

Simon Huisman
Enschede, January 2010

# Contents

# Chapter 1

# Introduction

Light has become an important carrier for information in modern communication technology. For example, it can be used to read data from a Blu-ray disc, to transfer information through a fiber or to encrypt secrets on single photons.

There is a fast-growing interest in controlling light with nanophotonic materials. Light propagation in a nanophotonic material strongly differs from propagation through a homogeneous material because of interference on length scales of the order of a wavelength. Photonic crystals are a class of nanophotonic structures that control light propagation at a fundamental level. In this thesis, we study light propagation in silicon photonic crystals at near-infrared frequencies.

## 1.1 Photonic crystals

Photonic crystals are periodically ordered composite materials with a spatially varying dielectric constant with a periodicity of the order of a wavelength of light [1, 2]. It can be a two-dimensional or three-dimensional periodic structure that strongly affects the dispersion relation of light. Due to the periodic variation of the dielectric constant, the crystal possesses photonic band structures, analogous to electronic band structures in solid-state physics [3]. Spectral bands can emerge for which light cannot propagate inside such a structure due to Bragg diffraction. These frequency bands for light are called stopgaps. Stopgaps are for example used in photonic crystal waveguides in integrated optical devices [4] and optical microcavities [5].

By manipulating light propagation with photonic crystals, one can control the rate of spontaneous emission of light sources [1, 6]. Spontaneous emission is a fundamental quantum optical process driven by vacuum fluctuations. Spontaneous emission can be manipulated by controlling the LDOS [7]. The LDOS can be interpreted as the density of field modes at a certain location inside the structure [8]. The control of spontaneous emission is of importance for several applications, like the design of efficient minature LEDs and lasers [1], and the development of single-photon sources for quantum information processing [9].

For certain designs of photonic crystals, frequency bands are predicted for which the LDOS becomes zero in the entire structure; a stopgap is formed for light in all directions. This *forbidden zone* for light is called a photonic band gap. A photonic band gap is extremely interesting, since the absence of the vacuum field will inhibit spontaneous emission and alter quantum optical effects caused by the presence of the vacuum field

[10], like Casimir forces [11]. Much effort has been put in fabricating photonic band gap crystals, but no one has convincingly demonstrated its existence.

## 1.2 Outline of this thesis

Recently, novel silicon two-dimensional and three-dimensional photonic crystals have been developed in our group [12, 13]. These photonic crystals strongly interact with light for near-infrared frequencies. The three-dimensional photonic crystals, which are called inverse woodpile crystals, are extremely interesting since a broad photonic band gap is expected [13, 14, 15, 16]. The inverse woodpile crystals are fabricated from two-dimensional photonic crystals [12] and have a diamond-like symmetry [14]. The two-dimensional photonic crystal is also interesting to control light propagation; it can posses a two-dimensional band gap for TE polarized light. From the symmetry of the crystal lattice, a low-frequency diffraction peak is expected below simple Bragg diffraction [17]. This can have implications for crystallography using X-ray diffraction, gaps for phonons and even for superconductors, if the crystal has a low-symmetry lattice.

For both two-dimensional and three-dimensional crystals, we have studied the presence of *forbidden zones* for light by identifying stopgaps using reflectivity. We have experimentally investigated how spontaneous emission can be manipulated with two-dimensional photonic crystals.

Chapter 2 provides a theoretical background. The first section describes how stopgaps in the dispersion relation are formed and how these can be observed as stopbands in reflectivity measurements. The next section reviews the interaction between an emitter and a photonic crystal. In chapter 3 experimental aspects of this work are described. The first section describes the photonic crystals. The following sections present the experimental apparatus and methods for reflectivity and emission measurements. Chapter 4 presents polarization controlled reflectivity measurements in different directions for two-dimensional photonic crystals. The first section describes a theoretical analysis of the modified dispersion relation inside two-dimensional photonic crystals. The second section discusses experimental results. Chapter 5 shows polarization controlled reflectivity measurements in different directions for three-dimensional inverse woodpile crystals. The first section describes the calculated dispersion relation inside an inverse woodpile crystal. The next section presents reflectivity spectra. Chapter 6 describes novel emission experiments of quantum dots inside two-dimensional photonic crystals. The first section describes the experiment. The next section presents emission spectra. Chapter 7 presents the conclusions, suggestions for improvements, and an outlook for new research.

# Chapter 2

# Theory

Photonic crystals are composite materials with a spatially varying dielectric constant with a periodicity of the order of the wavelength of light[1, 2]. Due to interference, the dispersion relation of light in a photonic crystal is strongly modified. For example, frequency bands emerge in which light waves cannot propagate through the medium without severe attenuation. In this chapter, we describe briefly how these bands emerge and how these can be characterized.

## 2.1 Bragg diffraction and the von Laue condition

The fundamental mechanism determining the dispersion relation inside photonic crystals is due to interference. The Bragg condition describes scattering and propagation of any kind of wave phenomenon in a periodic lattice [3, 18]. Fig. 2.1($a$) illustrates the geometry for simple Bragg diffraction. Scattered light waves on a set of crystal planes interfere constructively if the Bragg condition is met:

$$m\lambda = 2dn_{\text{eff}}\cos(\theta) \tag{2.1}$$

where $m$ is an integer, $\lambda$ is the wavelength in vacuum, $d$ is the lattice spacing, $n_{\text{eff}}$ the effective refractive index and $\theta$ the angle of the incident wave with the normal to the lattice planes. Incident waves that satisfy the Bragg condition for a set of lattice planes are diffracted for a range of frequencies, forming a stopgap in the dispersion relation. A stopgap describes a frequency range for which no propagating modes are allowed in a direction of the periodic structure. The center frequency $\omega_{\text{center}}$ and the width of the stopgap $\Delta\omega$ can be calculated by solving the Maxwell's equations inside the photonic medium, analogous to solving the Schrödinger equation for electrons propagating in a solid-state crystal. Methods are described in [2, 19]. The interaction strength between light and a crystal increases with the dielectric contrast [10, 20]. The photonic strength $S$ can be physically defined as the polarizability per unit cell volume [21]. The photonic strength of a crystal can be gauged by the relative width $\Delta\omega/\omega_{\text{center}}$ of the main stopgap.

The solid lines in Fig. 2.1($b$) indicate the dispersion relation for light in a one-dimensional photonic crystal. At the Bragg condition ($k = \frac{\pi}{d}$), there exist two standing waves: one mostly in the medium with high refractive index and one mostly in the medium with low refractive index [2, 19]. These standing waves result in different frequencies of light, which form the edges of the stopgap $\Delta\omega$. Stopgaps are the result of destructive interference of Bloch modes inside the crystal. Therefore, 'true' stopgaps only exist in structures of infinite size. However, the modes in a structure of finite size can still be

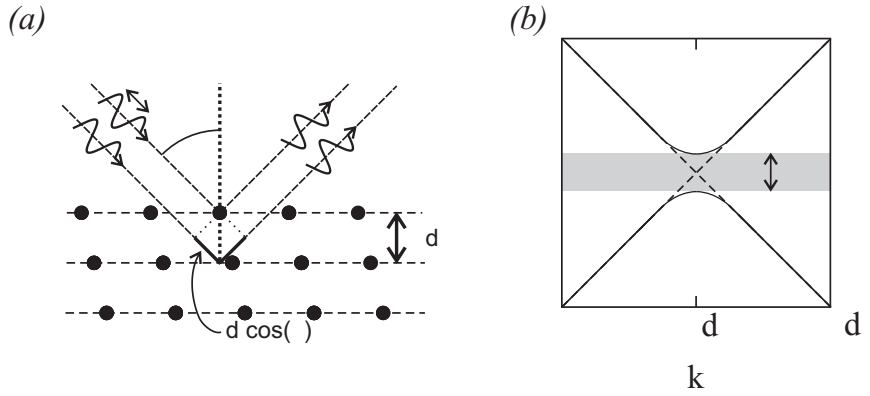


**Figure 2.1:** ($a$) Illustration of simple Bragg diffraction on a group of lattice planes with lattice spacing $d$. Constructive interference of the scattered waves occurs if the path length difference $2d\cos(\theta)$ between reflections from successive planes equals an integer number of wavelengths $\lambda$. ($b$) Dispersion relation along the normal to the lattice planes in ($a$). At the Bragg condition $k = \pi/d$, the dispersion relation (black) splits and forms a stopgap (grey area). In the limit of vanishing photonic interaction, the dispersion relation shows no stopgaps (dashed lines).

strongly suppressed, resulting in strong Bragg diffraction peaks. In real photonic crystals, the width of reflectivity peaks are called stopbands to indicate the difference from infinite and perfect structures.

An alternative formulation for diffraction of waves is provided by the von Laue condition [3, 22, 23]. The von Laue approach differs from the Bragg approach in that no particular sectioning of the crystal into lattice planes is singled out, and no ad hoc assumption of specular reflection is imposed. One regards the crystal as composed of identical microscopic objects placed at the sites of a Bravais lattice, each object can scatter the incident radiation in all directions. Constructive interference occurs in directions and at wavelengths for which the radiation scattered from all lattice points interfere constructively. This occurs when the difference between the incident wave vector $\mathbf{k}_{\text{in}}$ and outgoing wave vector $\mathbf{k}_{\text{out}}$ is equal to a reciprocal lattice vector $\mathbf{G}$:

$$\mathbf{k}_{\text{out}} - \mathbf{k}_{\text{in}} = \mathbf{G} \tag{2.2}$$

This condition is called the von Laue condition and describes diffraction of waves in reciprocal space. The von Laue condition is satisfied at certain planes in reciprocal space, called Bragg planes. Wave vectors $\mathbf{k}_{\text{in}}$ and $\mathbf{k}_{\text{out}}$ satisfy the von Laue condition if the tip of the vector lies in a plane that is the perpendicular bisector of a line joining the origin of reciprocal space to a reciprocal lattice vector $\mathbf{G}$. It can be shown that the Bragg and von Laue condition formulate equivalent diffraction conditions for crystals [3], with the Bragg condition acting in real space and the von Laue condition in reciprocal space. In reciprocal space, the points on the boundary of the Brillouin zone, which is enclosed by Bragg planes, are special because every wave with a vector extending from the origin to the zone boundary both satisfies the von Laue condition and Bragg condition.

However, diffraction become more complex in the case of multiple Bragg wave coupling. Van Driel and Vos [24] have shown that with increasing photonic interaction and increasing frequency, light can diffract from more than one set of lattice planes simultaneously. Such multiple Bragg diffraction results in band repulsions between Bloch states, causing the frequencies of the edges of the stopgaps to become independent of angle of incidence. In reciprocal space, this can occur at a corner of the Brillouin zone edge at

the intersection of multiple Bragg planes. We demonstrate experimentally in Chapter 4 reflectivity measurements on a structure where one can clearly distinguish multiple-Bragg diffraction from simple-Bragg diffraction.

In the limit of strong photonic interaction, many Bloch states interact so strongly that the edges of the stopgaps hardly vary for all propagation directions. This results in a common gap for all directions and all polarizations: a photonic band gap [24, 25].

From this section it becomes clear that stopgaps in the dispersion relation can be probed by diffraction measurements, indicating stopbands. Stopbands are experimentally observed frequency regions for which light cannot propagate. We will use this technique to study stopgaps for strongly interacting two-dimensional and three-dimensional photonic crystals. For a photonic band gap, no light for a certain frequency range can couple in any direction and therefore a diffraction peak appears in all directions. However, a reflectivity peak can also occur when an incident wave cannot (optimally) couple to a field mode in the crystal [2, 26]. Therefore, reflectivity measurements in combination with a calculated dispersion relation is not a convincing demonstration of a photonic band gap. One also needs to demonstrate that the light field is indeed forbidden inside the structure. A method for this is described in the next section.

## 2.2 Spontaneous emission and the local density of states

The emission of light is described by the transition of an emitter from a higher energy state $|e\rangle$ with energy $E_e$ to a lower energy state $|g\rangle$ with energy $E_g$ under perturbation of the light field. The difference energy $\hbar\omega_{eg}$ between the two states is carried by the creation of an energy quantum inside the interacting field mode, called a photon. Light emission can even occur when the interacting mode is in the vacuum state; this phenomenon is known as spontaneous emission [11, 27]. Spontaneous emission originates from fluctuations in the vacuum field. The probability for an emitter to decay depends on the number of field modes that can interact with the emitter placed at position $\mathbf{r}$. The local density of optical states (LDOS) defines the density of field modes $\rho(\mathbf{e_d}, \mathbf{r}, \omega)$ at this position that can interact with the emitter [8], where $\mathbf{e_d}$ is the orientation vector of the transition dipole. This approximation requires that the dielectric function $\epsilon(r)$ at this location is real, otherwise the LDOS is not defined [28]. If the LDOS can be controlled, one can control the emission rate (or emission probability) of light emission [1, 7].

In the weak light-emitter coupling regime [11], first order time-dependent perturbation theory can be used to describe the spontaneous emission rate. It is assumed that the emission of light originates from the interaction between an emitter and a field mode, which is given by the inner product of the electronic transition dipole moment and the electric field at position $\mathbf{r}$. The radiative decay rate $\gamma_{e\to g}$ is given by a modified version of Fermi's Golden Rule [29]:

$$\gamma_{e\to g}(\mathbf{r}, \mathbf{e_d}, \omega_{ge}) = \frac{\pi\omega_{ge}}{3\hbar\epsilon_0} \left|\langle g|\hat{\mu}|e\rangle\right|^2 \rho(\mathbf{e_d}, \mathbf{r}, \omega_{ge}) \tag{2.3}$$

where $\epsilon_0$ is the dielectric permittivity of the vacuum and $|\langle g|\hat{\mu}|e\rangle|$ is the transition dipole moment. The radiative decay rate of the emitter is given by the product of the transition dipole moment squared, which is purely a property of the emitter, and the LDOS $\rho(\mathbf{e_d}, \mathbf{r}, \omega_{ge})$, which is purely the fields determined by the surroundings of the emitter. In this approximation, the decay rate increases linearly with the LDOS.

Photonic crystals can strongly modify the dispersion relation of light and therefore the LDOS. The 'holy grail' is to develop and to demonstrate a geometry where the LDOS is zero. This range is the long-sought photonic band gap [1]. The ultimate goal would be to demonstrate the presence of a photonic band gap. Inside a band gap, spontaneous emission cannot occur since there are no light modes to couple. However, every crystal has a finite size and therefore the LDOS cannot be strictly zero. Calculations [30, 31] indicate that the LDOS decays exponentially with the crystal size, which leads to a way to distinguish a reduced LDOS from a band gap or some other effect such as a stopgap [32]. For frequencies outside band gap and stopgaps, an enhanced LDOS can be observed [6, 33, 34, 35], which enhances spontaneous emission.

The LDOS inside a photonic structure can be probed by embedding sources of spontaneous emission. One can measure fluorescence decay to determine the total decay rate $\gamma = \gamma_{\mathrm{rad}} + \gamma_{\mathrm{non,rad}}$, which is the sum of the radiative decay rate $\gamma_{\mathrm{rad}}$ and the non-radiative decay rate $\gamma_{\mathrm{non,rad}}$ [36, 37]. The non-radiative decay rate $\gamma_{\mathrm{non,rad}}$ is independent of the LDOS. The quantum efficiency of an emitter is defined as the ratio between the radiative decay rate and the total decay rate inside a homogeneous medium: $\eta = \frac{\gamma_{\mathrm{rad}}^{\mathrm{hom}}}{\gamma_{\mathrm{rad}}^{\mathrm{hom}} + \gamma_{\mathrm{non,rad}}}$. The quantum efficiency describes the ratio of the number of emitted photons per excited exciton. Depending on the quantum efficiency, changes in the LDOS appear in the measured decay curve in total emitted intensity[10].

For a single emitter, one would expect a single-exponential decay curve in the weak light-emitter coupling regime, since only one decay rate is present. In practice, one does not measure on a single emitter inside a crystal, but on an ensemble of emitters, where the location and orientation of emitters are distributed in some manner. Therefore, each emitter experiences a different LDOS. One typically measures a fluorescence decay curve that is non-exponential due to different decay rates [36]. From the measured decay curve, one can derive an averaged decay rate that is a measure for an average LDOS, as well on the width of the distribution [38].

The emission spectrum itself is also affected by the modified LDOS in a photonic crystal. Depending on the quantum efficiency and the emission spectrum of the emitters, one can expect the spectrum to show features related to the modified radiative decay rates. A reduced spectrum might for example be observed when a band gap is present. Moreover, the photonic structure also redistributes the emission due to stopgaps for propagation in certain directions, leading to angle dependent emission spectra [39].

# Chapter 3

# Experimental

We want to control the propagation of light with photonic crystals exhibiting stopgaps and band gaps. We demonstrate this control by reflectivity and emission measurements. We study two types of silicon photonic crystals: two-dimensional photonic crystals with a centred rectangular lattice and three-dimensional cubic inverse woodpile photonic crystals. The two-dimensional photonic crystal with a centred rectangular lattice is a macroporous photonic crystal that can have a two-dimensional band gap for TE polarized light and exhibits several stopgaps. The inverse woodpile crystal is a three-dimensional silicon photonic crystal that can posses a band gap for near-infrared frequencies. In this chapter, we describe the layout of these crystals. We also describe the setups and methods used for reflectivity and emission measurements.

## 3.1 Sample layout

### 3.1.1 Silicon two-dimensional photonic crystals with a centred rectangular lattice

The inverse woodpile structure is realized by first creating a macroporous two-dimensional photonic crystal with a centred rectangular lattice. We present both reflectivity and emission measurements on this type of crystal. The centred rectangular lattice is schematically shown in Fig 3.1($a$). A Scanning Electron Microscope (SEM) image is shown in ($b$). Air cylinders with radius $r$ are made with Reactive Ion-Etching (RIE). The centred rectangular unit cell has sides $a$ and $c$, with $a = \sqrt{2}c$. The pores are typically about 6 $\mu$m deep, $a = (693 \pm 10)$ nm, $c = (488 \pm 11)$ nm, $130 < r < 190$ nm. The tapering of the pores is smaller than $0.5^o$, except for about 1 $\mu$m at the bottom of the pores. Except for roughness near the entrance of the pores, the sidewalls of the pores are smooth on a scale below 50 nm. The properties of the pores and fabrication methods are described in [12, 13]. The two-dimensional crystal is cleaved parallel with the $a$-side of the unit cells for measurements in the $\Gamma K$-direction or cleaved parallel with the $c$-side for measurements in the $\Gamma M'$-direction[1].

### 3.1.2 Inverse woodpile photonic crystals

The inverse woodpile crystal is a cubic three-dimensional crystal with a diamond-like structure for which a broad band gap is expected [14, 15]. We present reflectivity measurements for this type of crystal. A schematic illustration of the lattice and the unit

[1] $\Gamma K$ and $\Gamma M'$ are defined in the reciprocal space of the lattice, see chapter 4

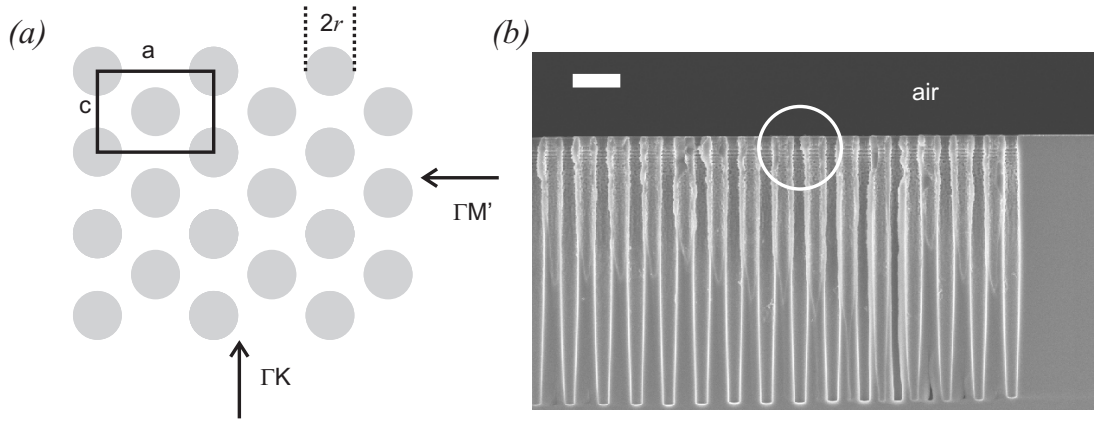


**Figure 3.1:** Schematic representation of the top of a two-dimensional photonic crystal with a centred rectangular lattice ($a$) and a SEM image of a crystal cleaved parallel to the $a$-side ($b$). In ($a$) grey circles with radius $r$ represent air holes etched in silicon. The solid rectangle marks a unit cell with lengths $a$ and $c$. In ($b$) a SEM image of a silicon two-dimensional photonic crystal with a centred rectangular lattice with $a = (693 \pm 10)$ nm, $c = (488 \pm 11)$ nm and $r = (181 \pm 11)$ nm is shown viewed perpendicular to the pores ($\Gamma K$-direction). The pore radius is determined near the center of the pores. The pores become more tapered close to the silicon. The silicon below the pores forms a good non-photonic reference for reflectivity measurements. Roughness appears near the entrances of the pores (marked with the white circle). The scale bar represents 1 $\mu$m.

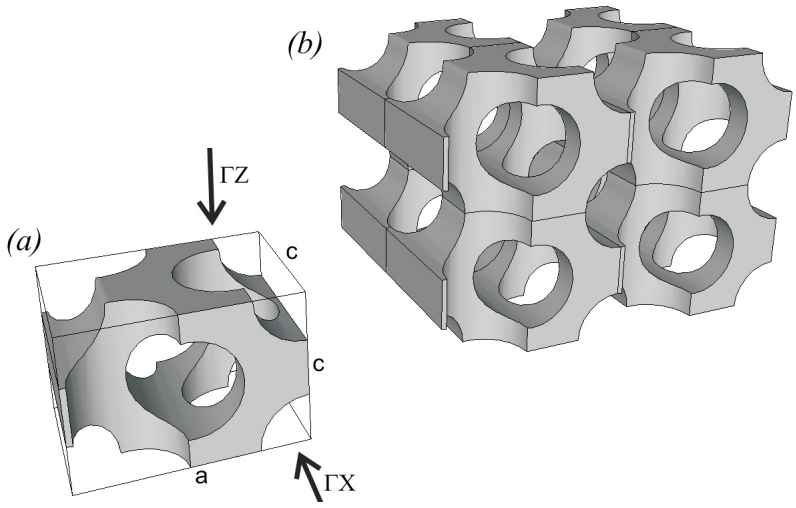


**Figure 3.2:** ($a$) Schematic representation of an orthorhombic unit cell of an inverse woodpile photonic crystal with dimensions scaled as $a = 690$ nm, $c = 488$ nm, with pore radius $r = 155$ nm. Viewed from the $\Gamma X$-direction, one gets the same unit cell as marked in Fig. 5.1($a$). ($b$) Inverse woodpile photonic crystal consisting out of eight unit cells. The $\Gamma X$-direction is parallel with the second set of etched pores, the $\Gamma Z$-direction is parallel with the first set.

cell of an inverse woodpile crystal are shown in Fig. 3.2. The inverse woodpile crystals we have fabricated are made of two interpenetrating two-dimensional photonic crystals. A schematic illustration of a part of a sample containing an inverse woodpile crystal is shown in Fig. 3.3. One starts with a silicon bar of about 0.5 mm $\times$ 0.5 mm and a length of the order of 1 cm, containing a cleaved two-dimensional photonic crystal. The two-

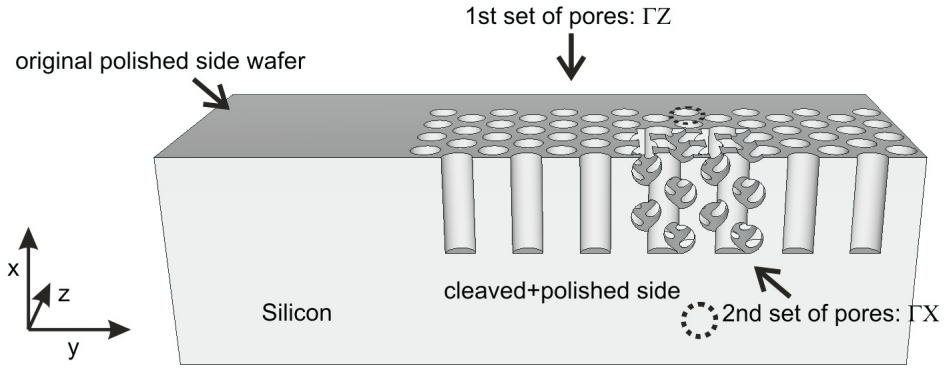


**Figure 3.3:** Schematic configuration of a sample with an inverse woodpile crystal. A silicon bar containing a cleaved two-dimensional photonic crystal with a centred rectangular lattice is polished. An identical second set of pores is etched perpendicular to the first set. The center of the pores of the second set are laterally aligned between the pores of the first set ($y$-direction). Depending on the lateral alignment of the second set of pores in the $x$-direction, the inverse woodpile crystal can have the same surface in both the $\Gamma X$- and $\Gamma Z$-directions. The dashed circles represent positions for collecting non-photonic reference spectra in reflectivity measurements.

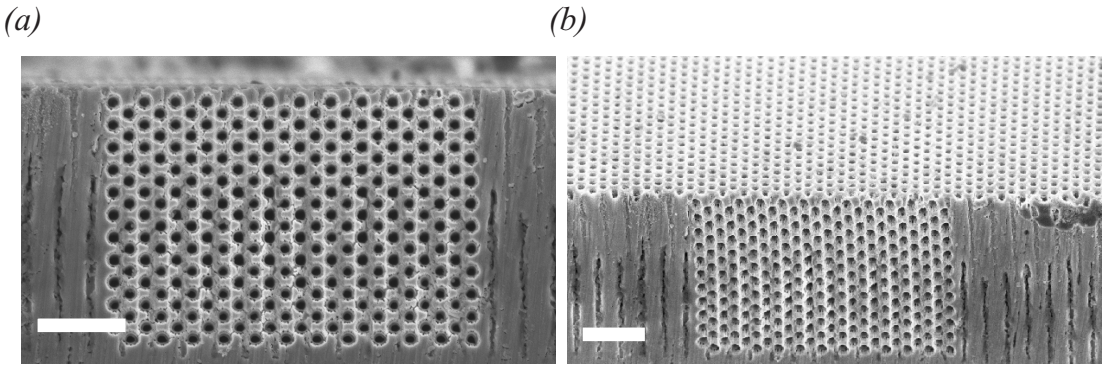


**Figure 3.4:** SEM pictures of an inverse woodpile crystal (Ad3b-14112008-3) with $a = (693 \pm 10)$ nm, $c = (488 \pm 11)$ nm and $r = (145 \pm 9)$ nm. ($a$) SEM picture parallel with the $\Gamma X$-direction, viewing a (110) surface of an fcc lattice. We observe that the centers of the second set of pores are aligned between the pores of the first set, like in Fig. 3.3. ($b$) Shows the same crystal viewed under an angle. The surface in the $\Gamma Z$-direction is different from the surface in the $\Gamma X$-direction. The scale bars represent 2 $\mu$m.

dimensional photonic crystal with a centred rectangular lattice is typically several mm long ($y$-direction in Fig. 3.3) and a mm wide ($z$-direction in Fig. 3.3). The cleaved side is polished to make the surface flat and parallel with the etched pores. A chromium layer is placed on top of the polished side and with Focussed Ion Beam (FIB) milling a mask for a second set of pores is made on a clean part of the sample. These pores have the same configuration as the first set of pores forming the original two-dimensional photonic crystal with a centred rectangular lattice. The pores of the original two-dimensional crystal are aligned in the $\Gamma Z$-direction of the inverse woodpile crystal, see Fig. 3.3. The second set of pores are aligned in the $\Gamma X$-direction of the inverse woodpile crystal. RIE is used to

create the second set of pores, where the centers of the pores are aligned exactly between columns of cylinders of the first set of pores, see Fig. 3.2($a$). After removing the mask, the crystal is ready for optical characterization. We have managed to fabricate inverse woodpile crystals of approximately 6 $\mu$m $\times$ 6 $\mu$m $\times$ 6 $\mu$m, limited by the resolution of FIB and the pore depth.

The advantage of our fabrication method is that one sample consists of a silicon bar with a large two-dimensional photonic crystal with a centred rectangular lattice, covering a length of several mm, and contains typically eight inverse woodpile crystals. We can select the best crystals from SEM pictures and confirm reproducibility of the measurements. The mask for each inverse woodpile crystal was made independently and therefore each crystal has a different lateral alignment in the $x$- and $y$-direction between the sets of pores.

The ratio $a = \sqrt{2}c$ is fixed in our fabrication scheme to form a face centred cubic lattice [13, 14, 15]. A band gap is expected between $0.14 < \frac{r}{a} < 0.30$ for a crystal of infinite size. A maximum relative width of the band gap of $\frac{\Delta\omega}{\omega} = 0.254$ is found at $\frac{r}{a} = 0.245$. For $\frac{r}{a}$ values increasingly further away from the optimal value, the relative gap width is reduced. The band gap edges move to higher frequencies with increasing $\frac{r}{a}$ [13].

SEM pictures of the best-aligned crystal are displayed in Fig. 3.4. We observe that the center of the second set of pores is aligned between the first set of pores. The interface of the surrounding two-dimensional photonic crystal is not as smooth as the crystal shown in Fig. 3.1($b$) due to polishing.

## 3.2 Reflectivity setup

A schematic drawing of the reflectivity setup is presented in Fig. 3.5 [17, 40]. A pulsed white light source (Fianium SC-450-2) with a frequency range of $450 - 2500$ nm is used as probe beam. After beam-expansion, the probe is polarized with a Glan Taylor calcite polarizer p1 (Thorlabs GT5). The probe is focused on the sample using a gold-coated dispersionless reflecting microscope objective (Ealing X74) with NA = 0.65. The beam waist of the focus is 1.2 $\mu$m at a wavelength of 633 nm [40]. The reflected light is

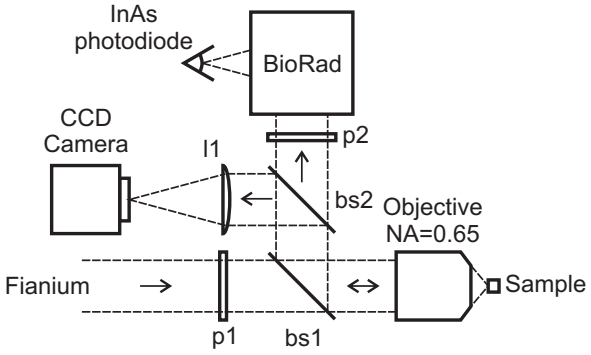


**Figure 3.5:** Schematic representation of the reflectivity setup. The expanded beam (dotted lines) from a broadband white light source (Fianium SC-450) is polarized with polarizer p1 and focused onto the sample using a gold-coated reflecting microscope objective (Ealing X74). The reflected light is collected with the same microscope objective, then spatially separated from the incident beam by pellicle beam splitter bs1. The spectrum is analyzed using an interferometer (BioRad FTS-6000) and an InAs photodiode. A fraction of the reflected light is imaged on a CCD camera with lens l1 and beam splitter bs2.

collected by the same objective and spatially separated from the probe beam with a pellicle beamsplitter bs1 (Thorlabs BP250, 50%/50% R/T). The reflected light is filtered in polarization with polarizer p2 (Thorlabs GT5) and analyzed using Fourier transform infrared spectroscopy [41, 42]. The interferometer is formed by a BioRad FTS-6000 in combination with a pre-amplified InAs photodiode. This setup is used to measure the reflectivity between 4000 and 12000 $cm^{-1}$ (between a wavelength of 0.83 and 2.5 $\mu$m) with a resolution of 32 $cm^{-1}$. The sample can be positioned with 50 nm accuracy using a translation stage and three motorized actuators. A halogen lamp can emit light along the probe path to illuminate the sample through the objective. Reflected light from the sample is collected by the microscope objective and focused onto a CCD camera by tube lens l1 with a focal length of 200 mm via beamsplitter bs1 and bs2 (Thorlabs BP208, 8%/92% R/T) [40].

### 3.2.1 Measurement procedure

We want to identify stopgaps and possible band gaps by observing diffraction peaks in the reflectivity. The reflectivity is obtained by normalizing the reflected spectrum of a sample to the reflected spectrum of a gold mirror with an average reflectivity above 95% (Thorlabs PF10-03-M01).

Objects were positioned in focus of the microscope objective by recording the spectra at multiple distances from the microscope objective, separated with steps of $(460 \pm 50)$ nm. The spectra were integrated between 5000 and 10000 $cm^{-1}$ and the signal is plotted versus the distance. The curve is fitted by a Gaussian function. The sample was positioned at the maximum of the Gaussian function. The actual focus is about 2 $\mu$m deeper inside the sample, which is well in the Rayleigh range for the wavelengths used [40].

When measured on a photonic structure, the sample is first placed in focus by collecting the reflectivity on a non-photonic part of the sample. For measurements on two-dimensional photonic crystals, the non-photonic reference is the silicon that surrounds the crystal. For inverse woodpile crystals, the non-photonic reference is surrounding silicon for measurements in the $\Gamma X$-direction and the top of a two-dimensional photonic crystal in the $\Gamma Z$-direction, see Fig. 3.3. The latter surface behaves as a medium with a constant effective refractive index when measured parallel with the pores, see insets of Fig. 5.3.

Gold spectra were collected before and after measuring on a sample. These spectra typically show minor differences, due to the good stability of the white light source and the setup. Therefore, the average gold spectrum is used for normalization. A good example of a reflectivity measurement on a two-dimensional photonic crystal in the $\Gamma M'$-direction is shown in Fig. 3.6. We observe minor differences between the spectra normalized to the average gold spectrum (black) and the individual gold spectra (grey). Other measurements show differences of maximum 3% absolute reflectivity, peak frequencies and widths remain unaffected.

We observe in ($b$) a rather constant non-photonic reference spectrum measured on silicon, with an average reflectivity of 27%. The reflectivity for well-aligned silicon is 31% and approximately constant in this frequency range. This is in agreement with the estimated reflectivity from Fresnel's equations for normal incidence [42], which gives approximately 32%. We believe that a fraction of the reflected light is not collected with the objective because of the alignment of the sample. The peak around 9400 $cm^{-1}$ is caused by the master source of the Fianium. Every reflectivity spectrum shows instabilities around this frequency. One sees a strong difference between the reflectivity of the photonic crystal in ($a$) and on the non-photonic reference ($b$).

The emitted light of the Fianium is approximately 90% parallel polarized with respect

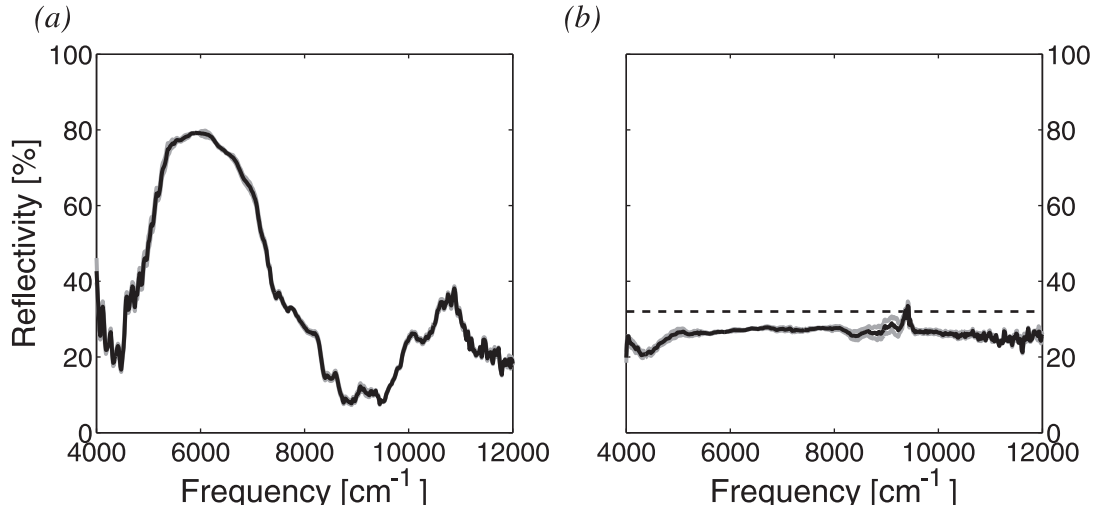


**Figure 3.6:** ($a$) Measured reflectivity for TE polarized waves in the $\Gamma M'$-direction of a cleaved two-dimensional photonic crystal with a centred rectangular lattice with $a = (693 \pm 10)$ nm, $c = (488 \pm 11)$ nm and $r = (155 \pm 8)$ nm. ($b$) Measured reflectivity from silicon close to the crystal. The graphs are normalized to the average gold spectra (black) and individual gold spectra (grey). The black dashed line indicates the reflectivity of bulk silicon predicted by theory, assuming normal incidence and constant refractive index.

to the optical table. Where possible, the polarization filters are fixed on horizontal polarization and the sample is rotated to determine the polarization of the incident waves relative to the sample. The collected spectra are at least averaged over 500 scans of the interferometer arm.

### 3.2.2 Extinction due to surface scattering and other effects.

A diffraction peak is theoretically expected to have a flat top with 100% reflectivity, that abruptly falls off at the edges. The width of the top is equal to the width of the stopgap, and the full width at half maximum is slightly larger. In presence of extinction, diffraction peaks become rounded and asymmetric with maxima less than 100%. The FWHM, however, remains the same [20]. Therefore, it is a reliable measure of the widths of stopgaps and is used throughout this thesis.

We expect the following sources of extinction in our experiments:

- All two-dimensional photonic crystals are cleaved. Some of these crystals are polished to fabricate inverse woodpile crystals. During the polishing step, the surface becomes rougher on a scale of 0.3 $\mu$m. For cleaved two-dimensional photonic crystals, the reflectivity can range up to 90 % for both polarizations. Photonic crystals that have been cleaved and polished afterwards have a reflectivity up to 80 %.

- The walls of the pores are "scalloped" near the entrance [12], see Fig. 3.1($b$). This roughness is also present at the pores in the second etch direction for inverse woodpile crystals. The reflectivity for inverse woodpile crystals is always measured parallel with a pore direction and therefore this roughness will be a source of extinction.

- Contamination of the surface by (small) particles causing scattering and absorption. We minimize this effect by selecting a clean part of the surface using microscope images.

- The photonic crystals are located near bulk silicon, which has a higher refractive index. A fraction of the light might be guided into the silicon, appearing as an additional loss. We will see that this effect is negligible.
- Losses can occur due to the interface of the photonic crystal; the interface behaves as a grating. This grating diffraction at the crystal interface appears for wavelengths shorter than the apparent crystal period at the interface. Both for the $\Gamma M'$-direction and $\Gamma K$-direction, the apparent crystal period is smaller than the wavelengths considered and will most likely not be important. Rowson et al. [43, 44] studied by FDTD simulations how the interface of the surface affects reflectivity. Similar analysis can be done for this type of crystals, but is beyond the scope of this work. In general, the reflectivity was position-independent for well-cleaved crystals.

## 3.3 Emission measurements

### 3.3.1 Setup

Fig. 3.7 shows a schematic overview of the setup used for emission experiments. A detailed description is provided in [45]. This setup has been developed to measure emission spectra and decay rates of emitters for near-infrared frequencies. We can choose between two excitation paths with flip mirror m1. In the case of excitation path 1, the same NA = 0.70 objective is used to excite the emitters and to collect the emitted light. In the case of excitation path 2, a separate NA = 0.05 objective is used to excite the emitters.

The remaining excitation light is filtered from the emitted light using a dichroic mirror (bs1) and two long pass filters (f1 and f2). We can also choose to filter the emission light on a specific polarization using polarizer p1. The filtered emission light enters a spectrograph (PI/Acton, SP2558) containing a 95 g/mm, 1.35 $\mu$m blazed grating, with a resolution of 1.4 nm. With a flip mirror inside the spectrograph, one can project the beam on a nitrogen cooled InGaAs Line detector to collect the emission spectrum. One can also direct the beam on a photomultiplier tube (PMT, Hamamatsu, H10330-75). The PMT is connected to a counting module (Picoquant, PicoHarp300), which can be used for time correlated single photon counting. With a pulsed excitation laser, we can perform time-resolved fluorescence measurements to obtain a fluorescence decay curve. The CCD camera can be used to obtain an image of the focal plane of both objectives.

### 3.3.2 Light sources

An Evidot-1500 lead sulphide (PbS) quantum dot suspension is used for emission experiments inside photonic crystals. An emission spectrum of the quantum dots inside a $4 \cdot 10^{-7}$ M toluene suspension is shown in Fig. 3.8. The quantum dots have an emission maximum at 1470 nm. The different sizes of the quantum dots causes the broadened spectrum.

The fluorescence decay rate of the same suspension is shown in Fig. 3.9. The quantum dots were excited with a frequency doubled $Nd^{3+}$:Yag laser (Time-Bandwidth, Cougar) with an emission wavelength of 532 nm, repetition rate of 204 kHz and a pulse width of 11 ps. As expected, the fluorescence decay can be well described by a single-exponential decay with a decay rate of $\gamma = (1.58 \pm 0.01)\ \mu s^{-1}$ ($\chi^2_{red} = 1.000$), where the error is given by the standard deviation of the fit. The quantum efficiency of these quantum dots is unknown, see Appendix A.

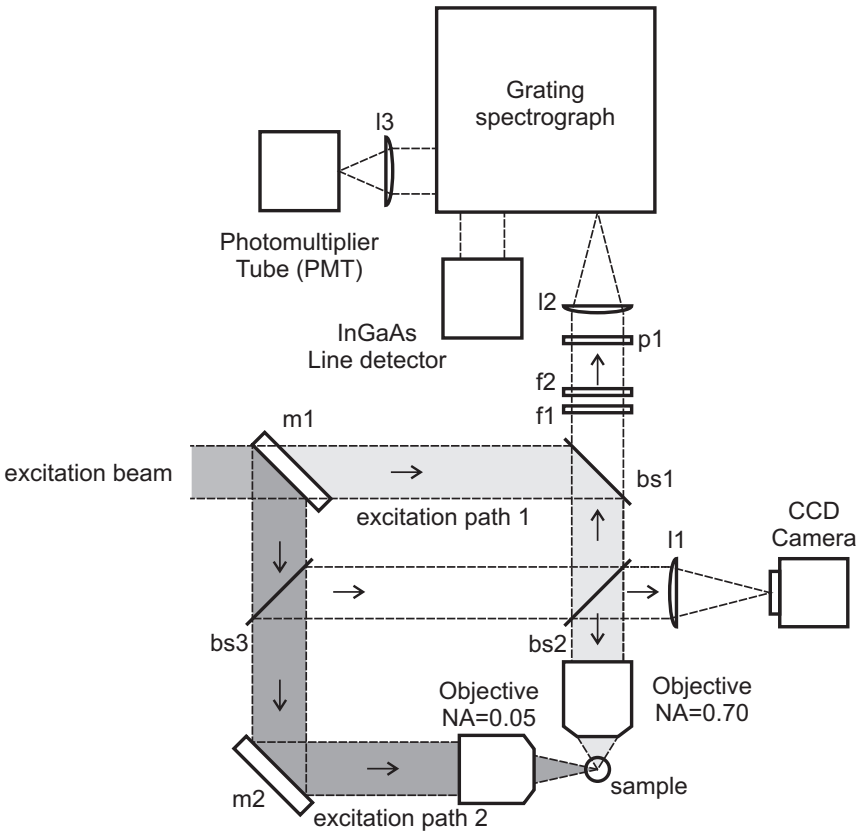


**Figure 3.7:** Schematic representation of the setup used for emission experiments. One can use the same objective for exciting the quantum dots and to detect the emitted light (excitation path 1) or one can choose a separate objective for exciting the quantum dots (excitation path 2).

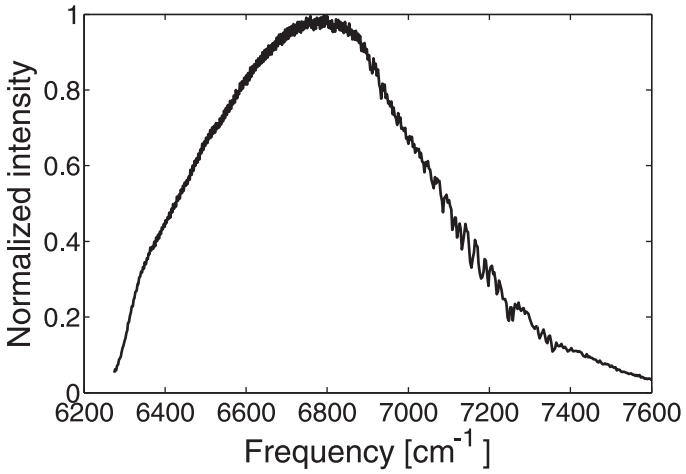


**Figure 3.8:** Emission spectrum measured for a $4 \cdot 10^{-7}$ M Evidot-1500 PbS quantum dot suspension in toluene.

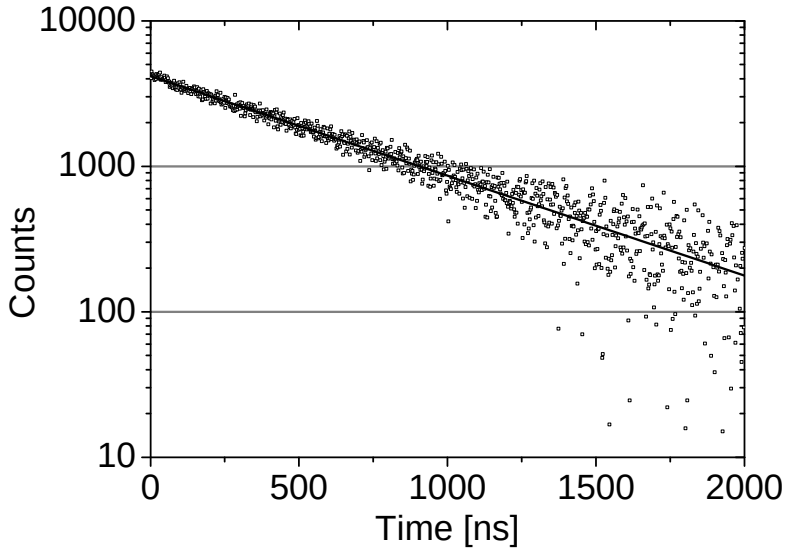


**Figure 3.9:** Fluorescence decay curve measured on a $4 \cdot 10^{-7}$ M Evidot-1500 PbS quantum dot suspension in toluene. The black line is a fitted single exponential decay.

# Chapter 4

# Reflectivity of silicon two-dimensional photonic crystals

In Sec. 3.1 we have described silicon two-dimensional photonic crystals that interact with light for near-infrared frequencies. This type of macroporous photonic crystals with a centred rectangular lattice are an interesting structure to control light propagation; it can posses a two-dimensional band gap for TE polarized light. From the symmetry of the crystal lattice we expect surprisingly a lower-frequency diffraction peak than for simple Bragg diffraction in the $\Gamma K$-direction [17]. This sub-Bragg diffraction peak should disappear for the $\Gamma M'$-direction. In this chapter, we study light propagation inside these crystals by identifying stopgaps using reflectivity.

Our experiment is similar to the experiment described by Schilling et al. [46] where they have measured reflectivity for a triangular lattice of macroporous silicon photonic crystals in the $\Gamma M$-direction for near-infrared frequencies. Rowson et al. [43, 44] measured reflectivity of a triangular lattice in both the $\Gamma K$- and $\Gamma M$-direction for mid-infrared frequencies. The first reflectivity spectra of these two-dimensional photonic crystals were measured in the $\Gamma K$-direction and demonstrated high reflectivity and peak width, but did not include the polarization dependence of light propagation [12, 13].

In our work we present polarization controlled reflectivity measurements in the $\Gamma K$- and $\Gamma M'$-directions on two-dimensional photonic crystals with a centred rectangular lattice. Our work is unique for experimentally observing a sub-Bragg diffraction peak. We investigate theoretically and experimentally how reflectivity peak-frequencies shift for varying pore diameters and identify stopgaps. We also studied how the longitudinal shape of the pores affects the reflectivity.

## 4.1 Diffraction theory for silicon two-dimensional photonic crystals

The photonic crystal is schematically represented in Fig 4.1 in real space ($a$) and reciprocal space ($b$). Air cylinders with radius $r$ are etched in the corners and center of the rectangular unit cell with sides $a$ and $c$, with $a = \sqrt{2}c$. The first Brillouin zone (grey) and neighbouring zones are illustrated in ($b$). The reflectivity is measured from the $\Gamma K$- and $\Gamma M'$-direction. The relevant Bragg planes and corresponding crystal planes for simple Bragg diffraction are shown.

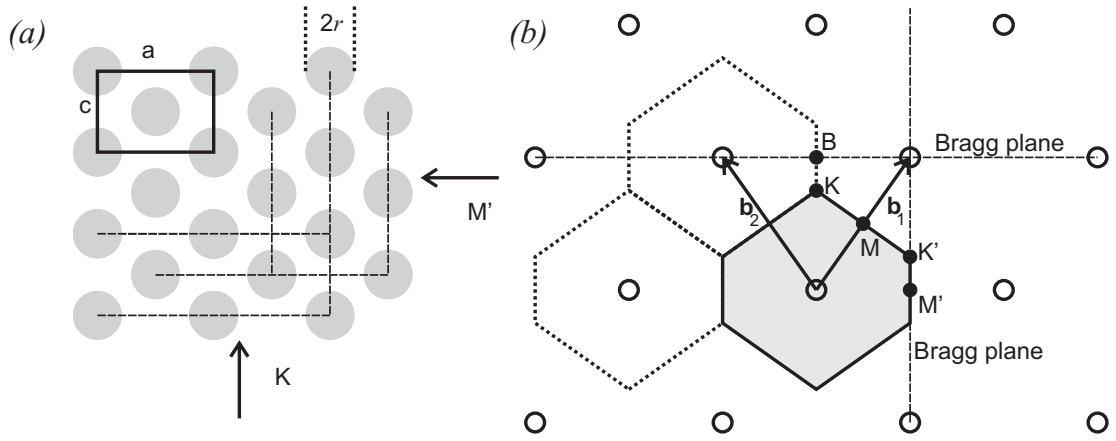


**Figure 4.1:** Schematic representation of a two-dimensional photonic crystal with a centred rectangular lattice in real space ($a$) and reciprocal space ($b$). In ($a$) grey circles with radius $r$ represent air holes etched in silicon. The solid rectangle marks a unit cell with lengths $a$ and $c$. Dashed lines show relevant crystal planes for simple Bragg diffraction parallel to the $\Gamma K$- or $\Gamma M'$-direction. In ($b$) the first Brillouin (grey) and neighboring Brillouin zones (dotted) are illustrated. Γ, K, K′, M, M′ and B are points of high symmetry of the Brillouin zone. The dashed lines are Bragg planes for simple Bragg diffraction in the $\Gamma K$- or $\Gamma M'$-direction.

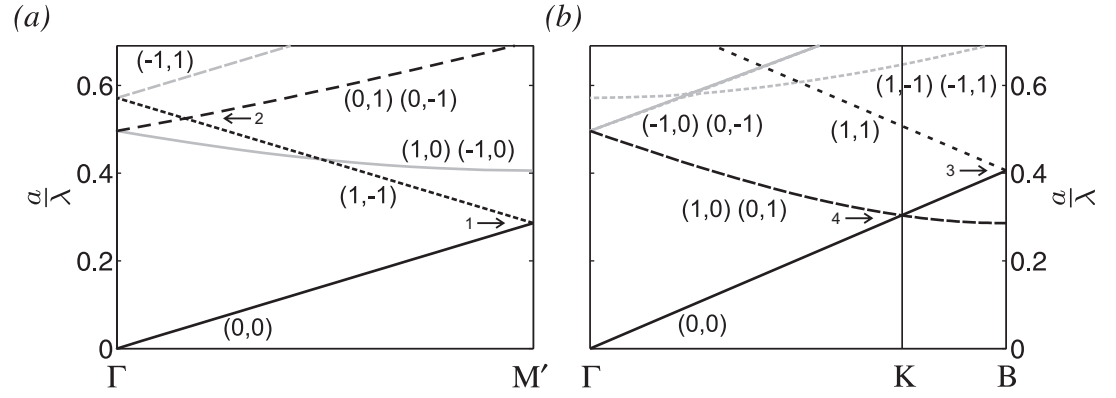


**Figure 4.2:** Calculated dispersion relations for optical modes in the $\Gamma M'$- ($a$) and $\Gamma K$-directions for an infinite silicon two dimensional photonic crystal in the limit of no interaction ($a$ = 690.6 nm, $c$ = 486.3 nm, $r$ = 1 nm, $\epsilon_{air} = 1$ and $\epsilon_{Si} = 12.25$, calculated with the MIT Photonic Bandgap Package). Note that both horizontal axes have the same site, however $\sqrt{2}|\Gamma M'| = |\Gamma B|$.

### 4.1.1 Dispersion relation in case of no interaction

The following is based on the description by Hartsuiker et. al [17] where the dispersion relations of a square and centred rectangular lattice are compared. The square lattice has a higher symmetry for which no sub-Bragg diffraction peak is expected, in contrast to the centred rectangular lattice for which a lower-frequency diffraction peak is expected than for simple Bragg diffraction.

The dispersion relation for a centred rectangular lattice with no interaction with the light field for instance occurs when the pore radius vanishes; $r = 0$. The dispersion relations in the limit of zero interaction for the $\Gamma M'$- and $\Gamma K$-direction are illustrated in Fig. 4.2 ($a$) and ($b$) respectively. The band coordinates in the bandstructure are given

as Miller indices $(hk)$, which correspond to reciprocal lattice points $\mathbf{G}_{hk} = h\mathbf{b}_1 + k\mathbf{b}_2$ in Fig. 4.1$(b)$. In this manner, one can identify how the dispersion relation is affected by neighbouring Brillouin zones. For the $\Gamma M'$-direction, the 00-band and the $1\bar{1}$-band cross at the edge of the Brillouin zone (Fig. 4.2, arrow 1). This crossing is the origin of the stopgap that opens if the interaction strength becomes non-zero [21, 25]. From Fig. 4.1 it is evident that a wave with a wavevector starting from $\Gamma$ extending to $M'$ both satisfies the von Laue condition and Bragg condition for simple Bragg diffraction [3, 23]. This would result in one diffraction peak for the equivalent diffraction conditions.

The third set of crossing bands close to the edge of the Brillouin zone (Fig. 4.2, arrow 2) are the 01- and $0\bar{1}$-bands and the $1\bar{1}$-band, resulting in a multiple Bragg condition. As the interaction strength is increased, these bands start to repel the other bands, forming a higher order stopgap [24], which appears as a diffraction peak.

For the $\Gamma K$-direction, the $K$-point satisfies the von Laue condition, since it is located on two crossing Bragg planes at the edge of the Brillouin zone. However, the Bragg condition for simple Bragg diffraction is not met at the edge of the Brillouin zone, but halfway the reciprocal lattice vector $\mathbf{G}_{11}$ in the Bragg plane through $B$, see Fig. 4.1$(b)$. This is where the 00- and 11-bands cross and form a stopgap (Fig. 4.2, arrow 3).

The 10- and 01- bands cross with the 00-band at the edge of the Brillouin zone in the $K$-point (Fig. 4.2, arrow 4), resulting in multiple Bragg diffraction. If the interaction strength is increased, these bands repel and a gap opens at the $K$-point. The multiple Bragg diffraction in the $K$-point still satisfies the von Laue condition, but is not located on the Bragg-plane associated with simple Bragg diffraction in the $\mathbf{G}_{11}$-direction.

Therefore, two different diffraction peaks are expected for reflectivity measurements in the $\Gamma K$-direction. The peak with the lowest frequency corresponds with diffraction on the $K$-point, satisfying the von Laue condition causing multiple Bragg diffraction. This diffraction peak has surprisingly a lower frequency than the second diffraction peak that corresponds with simple Bragg diffraction at the $B$-point.

### 4.1.2 Dispersion relation in case of interaction

Fig. 4.3 shows calculated dispersion relations for optical modes in a silicon two-dimensional photonic crystal for TE and TM polarized waves, with $\frac{r}{a} = 0.225$. This bandstructure is analysed in this part to predict stopbands in the experiment. Figures $(a)$ and $(c)$ show calculated bandstructures along points of high symmetry in the Brillouin zone in Fig. 4.1$(b)$. Figures $(b)$ and $(d)$ explicitly show bandstructures along the $\Gamma K$-direction until the $B$-point, for which a diffraction peak is expected at lower frequencies than for simple Bragg diffraction. The left vertical axis shows predicted frequencies in $\mathrm{cm}^{-1}$ and the right vertical axis shows corresponding normalized frequencies ($\frac{a}{\lambda} = \frac{\omega a}{2\pi c}$). The graphs contain dashed lines to indicate extrapolated Bragg conditions based on the long-wavelength limit of light dispersion. Only first order Bragg conditions in the $\Gamma M'$- and $\Gamma K$-directions are shown. Stopbands are expected at the frequencies of stopgaps.

Before the bandstructure is further analysed, we first have to consider experimental details. In the experiment we measure on a finite size crystal with imperfections using a NA = 0.65 reflecting objective. Therefore, the calculated band-structure can only be used as an indication where stopbands might occur. True stopgaps are never formed and therefore light will be weakly coupled into the crystal at these frequencies, reducing the reflectivity peaks. A measure for the distance that light can penetrate into the photonic crystal before being reflected by the lattice planes is given by the Bragg attenuation length

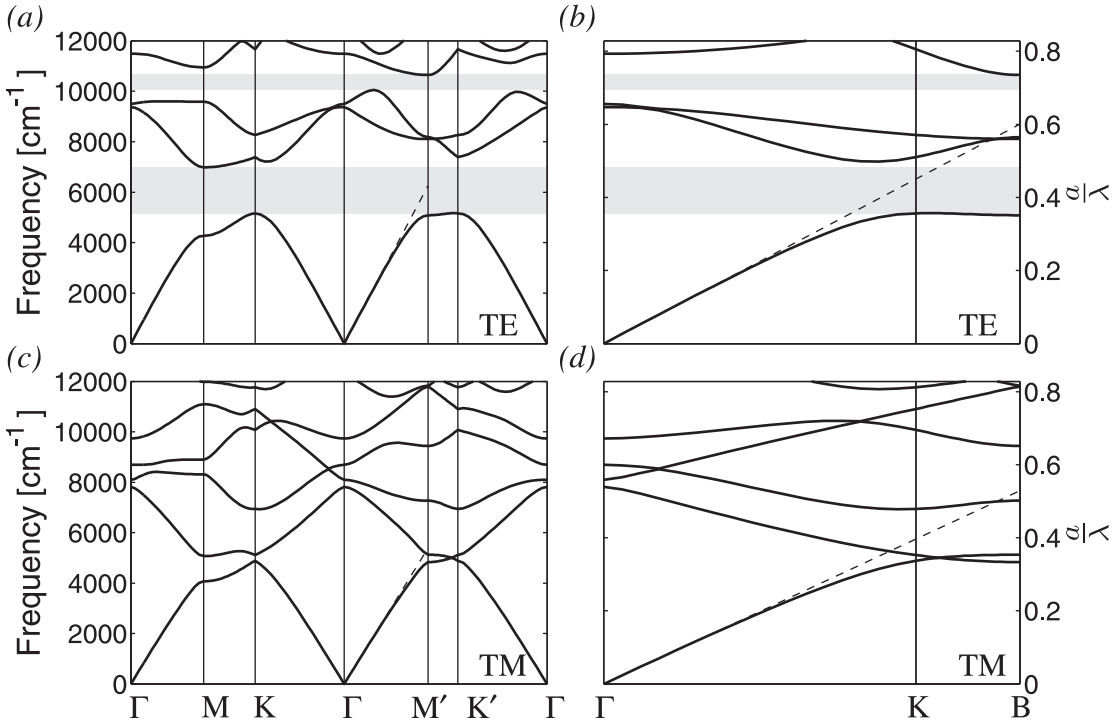


**Figure 4.3:** Calculated dispersion relations (solid lines) for optical modes in an infinite two-dimensional photonic crystal made of air holes in silicon ($a$ = 690.6 nm, $c$ = 486.3 nm, $r$ = 155 nm, $\epsilon_{air} = 1$ and $\epsilon_{Si} = 12.25$, calculated with the MIT Photonic Bandgap Package). Dispersion relations for TE and TM polarized waves in the first Brillouin zone are presented in ($a$) and ($c$) respectively. Bands in the $\Gamma K$-direction are extended to include first order Bragg conditions at the $B$-point in ($b$) and ($d$). Dashed lines crossing the $M'$- or $B$-point indicate first order Bragg conditions in the $\Gamma M'$- and $\Gamma K$-directions extrapolated from the long-wavelength dispersion. The grey areas mark two-dimensional band gaps for TE polarized light. The vertical axes in all the figures have the same scale.

$L_{\mathrm{B}}$ [10]:

$$L_{\mathrm{B}} = \frac{\lambda_{\mathrm{Bragg}}}{\pi S} \tag{4.1}$$

with $\lambda_{\mathrm{Bragg}}$ the central wavelength of the measured stopband and $S$ is the photonic strength, which is equal to the relative gap width $\Delta\omega/\omega_{\mathrm{center}}$.

Since the reflected light is collected and averaged over an incident angle up to approximately $\theta = 40^o$ to the normal, the band-structure has to be considered along multiple directions. In practice, when one measures from the $\Gamma K$-direction, one also has to consider the bandstructure along $\Gamma MK$. When one measures from the $\Gamma M'$-direction, one also has to take into account the bandstructure along $M'K'\Gamma$. To compare the bandstructure with this detail, one has to consider the bandstructure in a repeated zone scheme along the angles of incidence. One also has to take into account momentum conservation of the incident wavevector; the component of the wavevector parallel to crystal surface is equal to $\mathbf{k}_{\parallel} = \mathbf{k}_{in}\sin(\theta) = \left(\frac{\omega}{c}\right)\sin(\theta)$. Rowson et al. [43, 44] demonstrate how to take this effect into account for the $\Gamma M$-direction of a triangular lattice. Their results demonstrate that especially the lower order stopgaps are hardly affected by the angular spread of incident waves. This analysis is beyond the scope of this work. However, one can estimate for the $\Gamma K$-direction when the bandstructure along $KM$ has to be considered for an off-normal incident wave with $\theta = 40^o$. This occurs when the parallel component of this incident

wavevector has the same size as the projection of the $M$-point on the reciprocal vector $\Gamma M'$ in Fig. 4.1($b$), which is already the case at about 5600 cm$^{-1}$. Since we are interested in the frequency range between 4000 and 12000 cm$^{-1}$, we can expect to observe effects of the bandstructure along $KM$ for the entire frequency range. Following the same reasoning we can expect effects from the bandstructure along $M'K'$ for the whole range.

The frequency associated with the Bragg condition blue-shifts for off-normal incidence on a Bragg plane. Calculations for off-axis propagation out of the crystal plane have not been performed, but Rowson et al. [43, 44] have shown that for a triangular lattice the stopgaps slightly broaden and blue-shift for larger angles.

Now we analyse the dispersion relation in Fig. 4.3 in more detail. Below approximately 4000 cm$^{-1}$, the dispersion relation of light can be described as light propagation in a medium with a constant effective refractive index. Above 4000 cm$^{-1}$, the waves strongly interact with the lattice and stopgaps are formed. These stopgaps will appear as stop-bands.

**TE polarized light in the $\Gamma M'$-direction:** A first order stopgap is calculated between 5086 and 8106 cm$^{-1}$, which is part of the first order two-dimensional band gap for TE polarized light (grey area). This stopgap agrees with the extrapolated Bragg condition at 6266 cm$^{-1}$. There is a higher order stopgap between 10050 and 10650 cm$^{-1}$, part of a second two-dimensional band gap for TE polarized light (grey area). In the experiment we measure over a distribution of incident wave-vectors, therefore we also have to consider the gaps along $M'K'$. The lower-frequency gap is narrowed on the high frequency side and the higher-frequency gap broadens. Since the angle of incidence changes, the Bragg frequency blue-shifts for off-normal off-plane propagation.

**TM polarized light in the $\Gamma M'$-direction:** A first order stopgap is formed between 4832 and 5132 cm$^{-1}$, which is in agreement with the extrapolated Bragg condition at 5395 cm$^{-1}$. This gap narrows along $M'K'$. Higher order stopgaps are formed between 8095 and 8693 cm$^{-1}$ and 9654 and 9732 cm$^{-1}$.

**TE polarized light in the $\Gamma K$-direction:** A first order stopgap is formed between 5162 and 7211 cm$^{-1}$, which is part of the first order two-dimensional band gap. This gap becomes wider on the low-frequency side when the spread of incident wavevectors are considered (see bandstructure along $\Gamma MK$ in Fig. 4.3 ($a$)). This gap is not in agreement with the extrapolated Bragg condition at 8695 cm$^{-1}$, as expected from the difference in the $K$-point and $B$-point. A higher order stopgap is formed between 9496 and 10650 cm$^{-1}$.

**TM polarized light in the $\Gamma K$-direction:** Two bands cross each other near the $K$-point at 5010 cm$^{-1}$, which forms a stopgap for higher $\frac{r}{a}$. This gap is not in agreement with the extrapolated Bragg condition at 7666 cm$^{-1}$. This gap appears broader when the angular spread of incident wavevectors are considered (see bandstructure along $\Gamma MK$ in Fig. 4.3 ($c$)). The bands cross each other at 8537 cm$^{-1}$, where a stopgap is present in $\Gamma M$-direction.

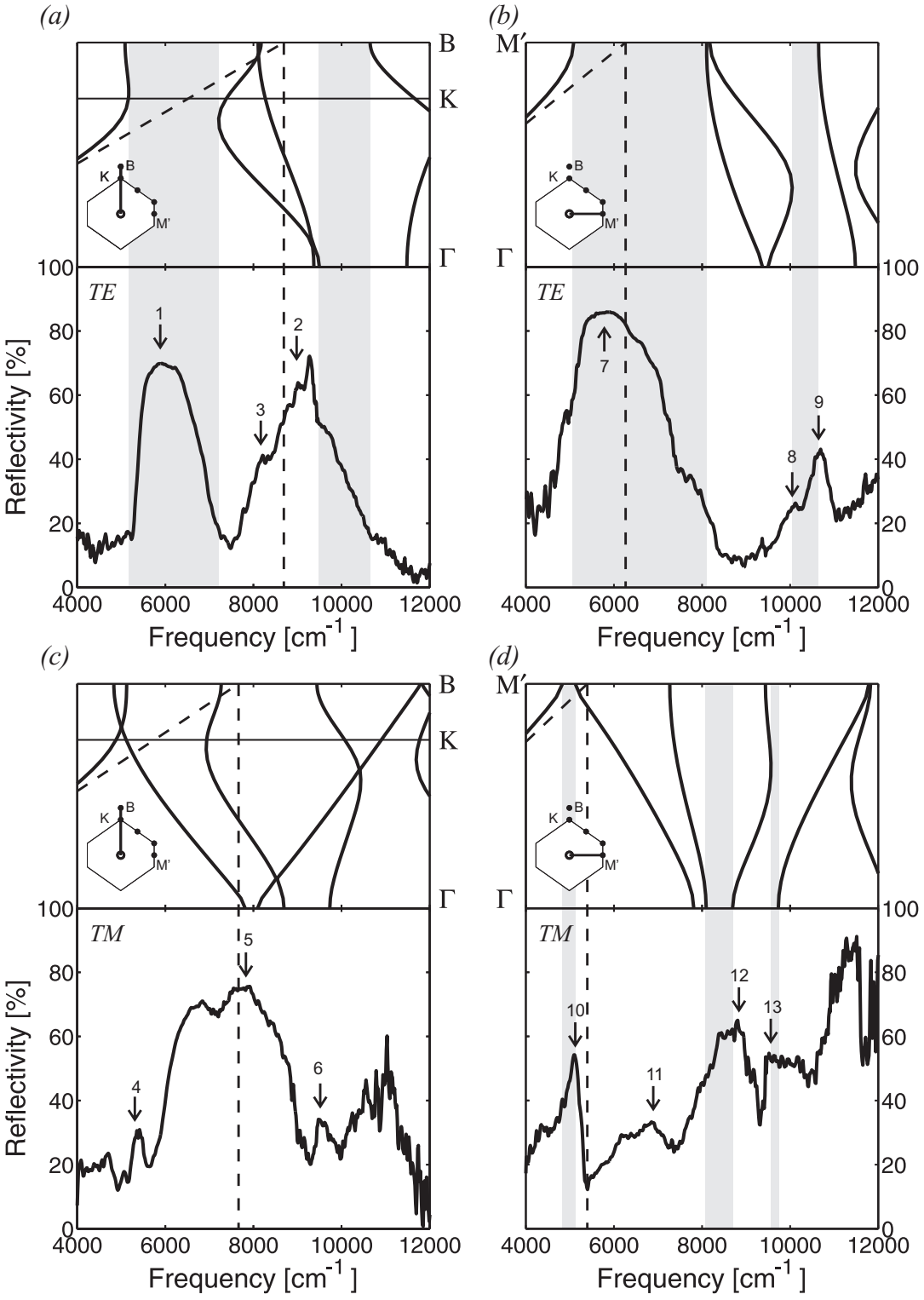


**Figure 4.4:** Comparison between calculated dispersion relations (solid lines top panels), first order Bragg conditions (vertical dashed lines) and measured reflectivity (bottom panels) for TE and TM polarized waves in the $\Gamma K$- $(a, c)$ and $\Gamma M'$-direction $(b, d)$ for a crystal with $r = (155 \pm 8)$ nm. Grey areas mark calculated stopgaps.

## 4.2 Results

### 4.2.1 Reflectivity spectra in the $\Gamma K$- and $\Gamma M'$-direction

Fig. 4.4 shows a comparison between measured reflectivity, calculated dispersion relations and extrapolated first order Bragg conditions for a crystal with $r = (155 \pm 8)$ nm for TE and TM polarized waves in the $\Gamma K$- and $\Gamma M'$-direction. The complete calculated bandstructure is also shown in Fig. 4.3. Both the peak reflectivity and peak widths are reproducible at different locations on the crystal. The shape of the reflectivity spectra is comparable for other crystals. The fluctuations in the spectra around 9400 cm$^{-1}$ are caused by the Fianium master source and will be neglected in analysis.

**TE polarized light in the $\Gamma K$-direction:** The first reflectivity peak at 5925 cm$^{-1}$ for TE polarized waves (arrow 1, Fig. 4.4($a$)) corresponds to a stopgap caused by multiple Bragg diffraction on the $K$-point. This diffraction peak satisfies the von Laue condition, but not the condition for simple Bragg diffraction. The second major peak at 9011 cm$^{-1}$ (arrow 2, Fig. 4.4($a$)) corresponds with a calculated stopgap and is caused by simple Bragg diffraction on the $B$-point, which is in agreement with the extrapolated first order Bragg condition. We experimentally observe a diffraction peak at a lower frequency than for simple Bragg diffraction.

For cleaved crystals, the reflectivity of both peaks can range up to 75%. For polished samples, the first reflectivity peak becomes typically 70%, however, the second peak is reduced to 40%, since scattering is stronger for higher frequencies. There seems to be a small peak at 8209 cm$^{-1}$ (arrow 3, Fig. 4.4($a$)), which might be caused by a flat band in the dispersion relation.

**TM polarized light in the $\Gamma K$-direction:** The first reflectivity peak for TM polarized light at 5354 cm$^{-1}$ (arrow 4, Fig. 4.4($c$)) agrees with two calculated crossing bands starting the formation of a narrow stopgap. This peak also agrees with a calculated stopgap along the $\Gamma MK$ in the calculated dispersion relation of Fig. 4.3($c$). Depending on the structure, this peak can range up to 60%, which was observed for a polished surface.

The broad reflectivity peak at 7870 cm$^{-1}$ (arrow 5, Fig. 4.4($c$)) is most likely caused by simple Bragg diffraction or bad coupling to crystal modes, which has typically an amplitude of 80% for both polished and cleaved samples. The peak at 9505 cm$^{-1}$ (arrow 6, Fig. 4.4($c$)) originates from a stopgap in the $\Gamma M$-direction, see Fig. 4.3($c$). Higher order peaks are not well understood, but might be caused by bands to which light cannot optimally couple or a stopgap in the $\Gamma M$-direction.

**TE polarized light in the $\Gamma M'$-direction:** The first major reflectivity peak at 5894 cm$^{-1}$ for TE polarized waves (arrow 7, Fig. 4.4($b$)) is caused by a stopgap satisfying both the von Laue and simple Bragg conditions. This peak clearly overlaps with the TE peak for the $\Gamma K$-direction (arrow 1, Fig. 4.4($a$)), confirming the presence of a two-dimensional band gap for TE polarized light. This peak can be 90%, but is typically around 80% reflectivity. The Bragg attenuation length is estimated smaller than 3 $\mu$m and therefore it is unlikely that the peak is affect by the finite size of the crystal. The reflectivity does not reach 100%, likely caused by the surface quality of the crystal. If a fraction of the light in general is lost by guidance into the silicon surrounding the crystal, this reflectivity peak shows that this can only be a small contribution.

The combined second and third peaks at 10120 and 10690 cm$^{-1}$ (arrows 8 and 9, Fig. 4.4($b$)) is in agreement with a higher order calculated stopgap. Depending on the

measurement position, this combined peak can range up to 40% reflectivity, but was typically around 30%. Spectra obtained on the same crystal are presented in Fig. 3.6 and 4.6, which are in excellent agreement.

**TM polarized light in the $\Gamma M'$-direction:** The reflectivity peak for TM polarized waves at 5108 cm$^{-1}$ (arrow 10, Fig. 4.4($d$)) is in agreement with a stopgap corresponding to von Laue and simple Bragg conditions and is typically 50%. The second peak at 6897 cm$^{-1}$ (arrow 11, Fig. 4.4($d$)) is not understood, but might be caused by a band to which light cannot optimally couple. The reflectivity of this peak is around 30% at the high frequency side. A similar peak is also observed by [46] for the triangular lattice. The peaks at 8811 and 9521 cm$^{-1}$ (arrows 12 and 13, Fig. 4.4($d$)) agree with higher order calculated stopgaps and are generally around 60%. The increased reflectivity above 10500 cm$^{-1}$ is not well understood, but is consistently present and partly corresponds to a stopgap in the $\Gamma K'$-direction, see $\Gamma K'$ in Fig. 4.3($c$).

In summary, for the $\Gamma K$-direction for TE polarized light a lower-frequency diffraction peak is observed below the diffraction peak corresponding to simple Bragg diffraction. This sub-Bragg diffraction peak disappears for the $\Gamma M'$-direction. This diffraction peak has implications for crystallography using X-ray diffraction; our results imply that extra diffraction peaks can appear for crystals with a lower-symmetry that the square lattice.

### 4.2.2 Peak frequency as a function of air pore radius

The reflectivity has been obtained for several crystals with a different pore radius $r$. Fig. 4.5 shows normalized measured frequencies and halfwidths of reflectivity peaks measured in the $\Gamma K$-direction and $\Gamma M'$-direction as a function of normalized pore radius. All points for a specific $\frac{r}{a}$ have been obtained from the same spectra. The presented spectra are reproducible for the specific pore radius. We compare obtained spectra with calculated stopgaps (grey surfaces) and extrapolated Bragg conditions (dashed lines). Hartsuiker et al. [17] compared the reflectivity peaks with Bragg conditions using the refractive index calculated with Maxwell-Garnett equations. From our measurements it follows that this comparison is accurate for TM polarized light, but inaccurate for TE polarized light.

Error bars are not included in Fig. 4.5. The error in $r$ is for every crystal 5%. Every crystal has been made using the same mask with $a = (693 \pm 10)$ and $c = (488 \pm 11)$ nm. Calculations have been performed with $a = 690.3$ nm and $c = 486.3$ nm. The errors in the frequencies on the vertical axis are spectra-dependent. Depending on the position that is measured, the peak width and peak position vary. The selected spectra are obtained with a resolution of 32 cm$^{-1}$ and vary in width of 200 cm$^{-1}$. The widths are obtained after correcting the spectra for the constant average background reflectivity. The stopgaps have been calculated in the $\Gamma K$-direction until the $K$-point.

**$\Gamma K$-direction:** The lowest frequency reflectivity peaks for TE-polarized light are in excellent agreement with the calculated stopgap. The peak widths are not exactly matching the widths of calculated stopgap, but the difference might be caused by angular spread of incident beams and the fact that the bandstructure between $KB$ was not included. This frequency peak cannot be explained with simple Bragg diffraction, but can be explained with multiple Bragg diffraction or von Laue diffraction. The higher order reflectivity peaks overlap well with the extrapolated Bragg condition and overlap partly with a calculated

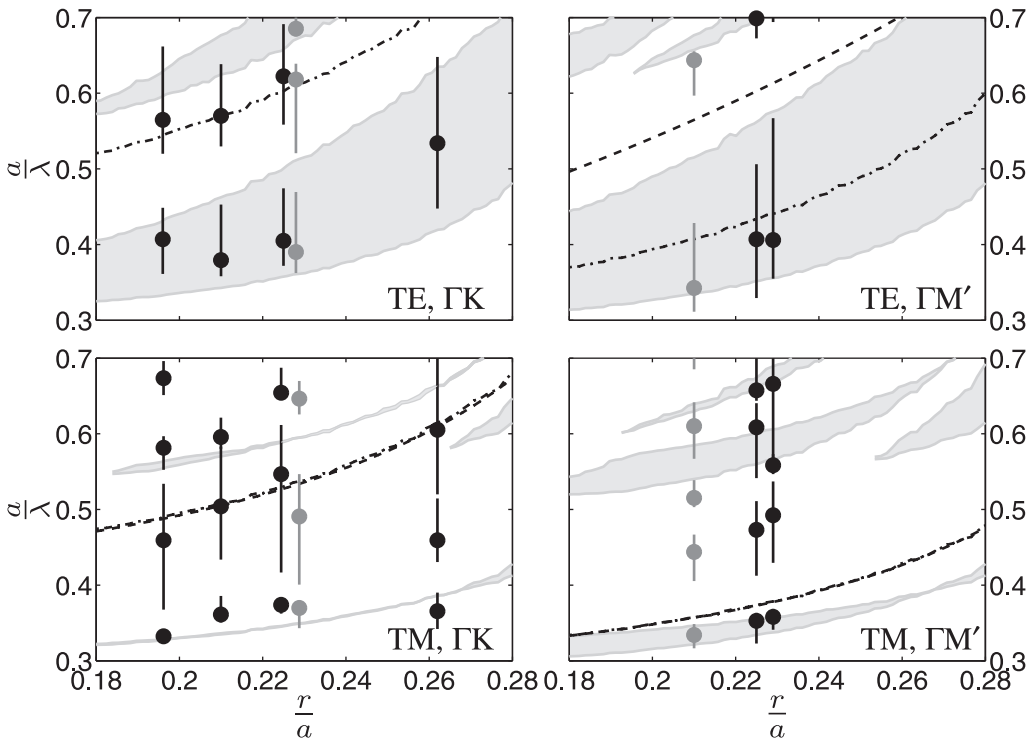


**Figure 4.5:** Normalized measured frequency (symbols) and half-widths (bars) of reflectivity peaks in the $\Gamma K$-direction and $\Gamma M'$-direction as a function of normalized pore radius for TE and TM polarized waves. Black symbols are measured with the BioRad interferometer, grey symbols are measured with the Interspec interferometer. Grey areas are stopgaps calculated with the MIT Photonic Bandgap Package. Dashed lines indicate the first order Bragg-condition, where the refractive index is estimated from Maxwell-Garnett equations. The dash-dotted lines are first order Bragg-conditions extrapolated from the long-wavelength regime of the calculated dispersion relations. The error on the horizontal axis is 5%.

stopgap. The Bragg condition predicted by the Maxwell-Garnett equation lies above the scale in this graph and therefore does not match the measurements.

The lowest frequency reflectivity peaks for TM polarized light are in reasonable agreement with the narrow calculated stopgap, which is caused by two crossing bands. The second lowest frequency reflectivity peaks are clearly in agreement with the extrapolated Bragg condition, which coincides with the Bragg condition predicted by the refractive index estimated from Maxwell-Garnett relations. These peaks cannot be explained by light propagating along the $\Gamma M$-direction, see Fig. 4.3. Higher order peaks are hard to compare, but might be caused by inefficient coupling on bands and observed stopgaps in the $\Gamma M$-direction.

**$\Gamma M'$-direction:** For TE polarized waves there is an excellent agreement with calculated stopgaps and measured reflectivity. Although the reflectivity peaks are narrower than the stopgaps, which can be explained by smaller stopgaps in the bandstructure in the $M'K'$-direction, the peak locations agree well with both calculated stopgaps and the extrapolated Bragg condition. No lower-frequency diffraction peak is observed below simple Bragg diffraction. We clearly see that the peaks for the lower frequency reflectivity peaks are

broader than for the $\Gamma K$-direction, which is in agreement with the calculated stopgaps. The Bragg condition based on the Maxwell-Garnett relations is not in agreement with the measured reflectivity.

The lowest reflectivity peaks for TM polarized waves are in agreement with the calculated stopgap and predicted Bragg conditions. The peak width is again broader than for the lowest peaks in the $\Gamma K$-direction. The second set of peaks is consistently present and is likely caused by an inefficient coupling to the bands. Higher order reflectivity peaks are in agreement with the calculated stopgaps.

We observe that the calculated dispersion relations along $\Gamma M'$ and $\Gamma K$ can be used to explain most of the reflectivity peaks. By considering also the dispersion along $\Gamma M$ and $\Gamma K'$ one can explain deviations from the measurements and predicted gaps.

It would be interesting if we could also measure the dispersion relation of the same crystal. One of these methods is to probe modes inside such a structure using reflectivity [47, 48, 49, 50]. Furthermore, Rowson et al. [43] describe for a triangular lattice finite difference time domain (fdtd) simulations to predict the reflectivity. They also make an analysis for off-axis and off-plane incidence reflections, by calculating the bandstructure with a plane-wave method. Similar analysis would improve our understanding of the reflectivity. This could also help to investigate to which modes light is coupled in our experiment, to distinguish stopbands from badly coupled modes.

### 4.2.3 Reflectivity affected by the shape of the air pores

The pores are not perfect smooth cylinders but are of finite depth and have a tapering angle of less than $0.5^o$ (except near silicon) [12], see Fig. 3.1($b$). Due to tapering, the air fraction is higher near the top surface of the crystal and therefore one might expect a small blue shift of the reflectivity when one obtains the reflectivity close to the top surface. We have studied how the reflectivity depends on the relative height on which the focus reflects on a photonic crystal. An example of such a measurement is shown in Fig. 4.6. These measurements were done on a cleaved structure in the $\Gamma M'$-direction for TE polarized waves. These measurements have been reproduced on polished samples in the $\Gamma K$-direction for both TM and TE polarized waves.

When the focus is still on silicon, a rather flat reflectivity is obtained of about 26%. On the interface between silicon and the photonic crystal, the background reflectivity reduces and reflectivity peaks start to form, since air pores are located inside the focus. When the focus is moved further on the crystal, the lower frequency peak gets broader and blue-shifts for TE polarized waves, since the filling fraction of silicon decreases. For TM polarized waves, the reflectivity peaks are approximately as wide everywhere on the crystal. The average background reflectivity decreases further until the center of the focus is at $x = 7$ $\mu$m in Fig. 4.6($a$). From that height, the sidewalls of the pores are smooth and straight, resulting in a constant width of the reflectivity peaks. Near the top surface, the reflectivity rapidly drops, but clearly does not blue-shift.

Therefore, we can conclude that tapering does not form a significant contribution to the position dependent reflectivity. The width of the peaks are position dependent near the edges of the pores.

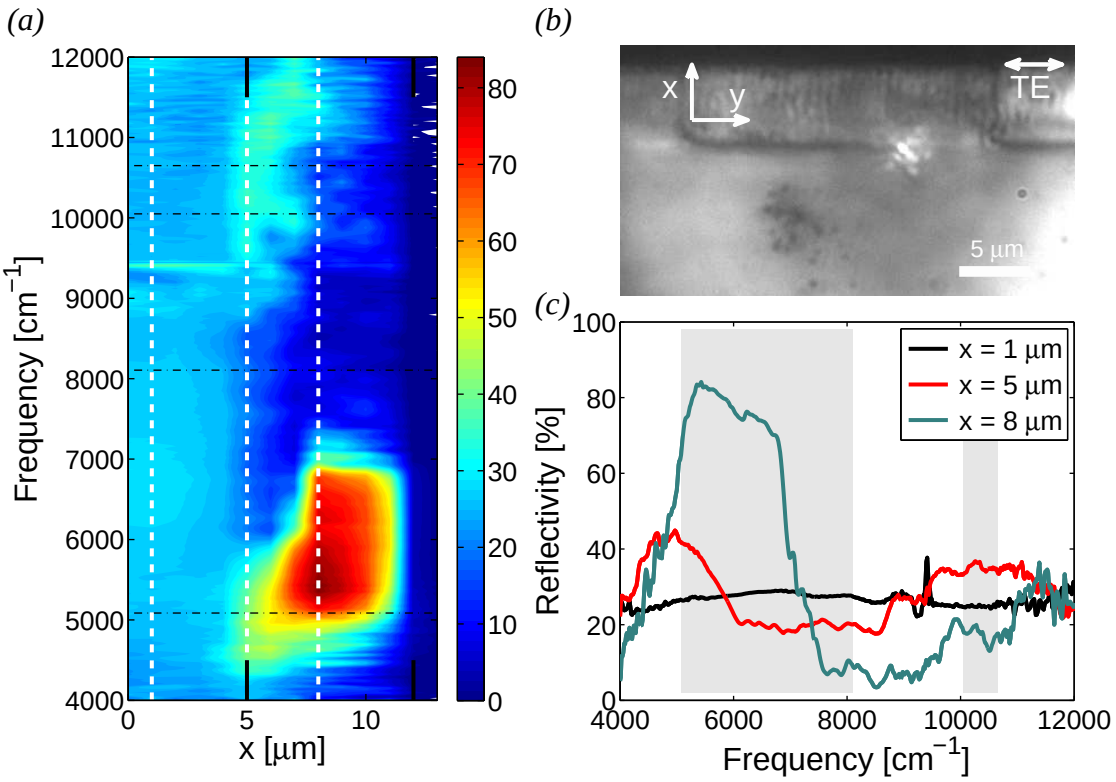


**Figure 4.6:** *(color)* X-scan at a different location over the same crystal as in Fig. 4.4(*b*) for TE polarized waves, measured in the $\Gamma M'$-direction. The scan started with the focus on the silicon ($x = 0$ $\mu$m), continued over the crystal ($6 < y < 12$ $\mu$m) and ended on air, and the sample was moved with steps of $(1.0 \pm 0.3)$ $\mu$m. (*a*) Collected spectra for several x-positions. The black lines on the horizontal axis indicate the boundaries of the crystal. The white dashed lines are spectra displayed in (*c*). The black dash-dotted lines indicate calculated edges of stopgaps in the $\Gamma M'$-direction. (*b*) Microscope picture of the crystal. (*c*) Three reflectivity spectra measured at the y-coordinates given by the white dashed lines in (*a*). The grey areas are calculated stopgaps.

## 4.3 Conclusions

We have studied the polarization dependent reflectivity of the silicon two-dimensional photonic crystals. We have clearly demonstrated for TE polarized light in the $\Gamma K$-direction a major diffraction peak which has a lower frequency than diffraction corresponding to simple Bragg diffraction. This sub-Bragg diffraction peak is not present for the $\Gamma M'$-direction, as expected from the symmetry of the lattice.

The measured spectra show high and broad peaks demonstrating that the crystals are of excellent quality. For the $\Gamma M'$-direction we have observed reflectivity peaks of 90% for cleaved crystals. The reflectivity was measured for crystals with a range of pore radii. The reflectivity peaks move to higher frequencies with increasing pore radius. The reflectivity peaks can be well explained with calculated dispersion relations and first order Bragg diffraction based on the long-wavelength limit of the dispersion relation. The overlap of the reflectivity peaks demonstrate a two-dimensional bandgap for TE polarized light; a two-dimensional *forbidden zone* for light.

We conclude that the widths of the reflectivity peaks remain constant along the longitudinal axis of the pores, except for positions close to the edges of the pores.

# Chapter 5

# Reflectivity of silicon inverse woodpile crystals

In our group we have developed silicon three-dimensional inverse woodpile crystals that strongly interact with light for near-infrared frequencies [13]. Depending on the parameters of the structure, this type of macroporous crystal has a photonic band gap with a width of approximately 25% for near-infrared frequencies [14, 15]. In this chapter, we investigate the band gap using polarization-resolved reflectivity spectra.

The first reflectivity measurements on silicon inverse woodpile crystals were performed by Schilling et al. [51]. A two-dimensional triangular lattice was used as a starting point to fabricate the inverse woodpile crystal. Unpolarized reflectivity measurements reveal a stopband along the direction of incidence, which corresponds with the bandstructure of the model, indicating the presence of a band gap. Other groups have fabricated inverse woodpile crystals of different materials using several methods, but the focus of their work was mainly on fabrication methods [52, 53]. The first reflectivity experiments on our structures were started by Woldering et al. [13].

Here we present polarization controlled reflectivity measurements in the $\Gamma X$- and $\Gamma Z$-direction for a range of pore diameters. We show overlapping reflectivity peaks from different directions and polarizations for one of the crystals, which is a signature of a photonic band gap. The reflectivity has been measured at several positions on the crystal surface to investigate reproducibility of the measurements and to study the influence of the crystal boundaries on the reflectivity. The silicon filling fraction of one of the crystals has been estimated from reflectivity in the $\Gamma Z$-direction.

## 5.1 Diffraction theory for silicon inverse woodpile crystals

Our design of the inverse woodpile photonic crystal is schematically shown in Fig 5.1 in real space ($a$) and reciprocal space ($b$). The crystal consists of two perpendicular, geometrically identical, sets of cylindrical pores. An individual pore set forms the lattice of the two-dimensional crystals described in Sec. 3.1, with $a = \sqrt{2}c$. The combination of the two sets results in a three-dimensional structure with a face centred cubic lattice, which is a diamond-like structure. A volume of high symmetry in reciprocal space is marked in ($b$), which is called the irreducible Brillouin zone of a simple orthorhombic lattice [13, 15]. Strictly speaking, this volume is not the Brillouin zone of the inverse woodpile crystal, since it is not the Wigner-Seitz cell of the reciprocal lattice. Calculated dispersion relations for this volume describe the dispersion relation for the entire lattice.

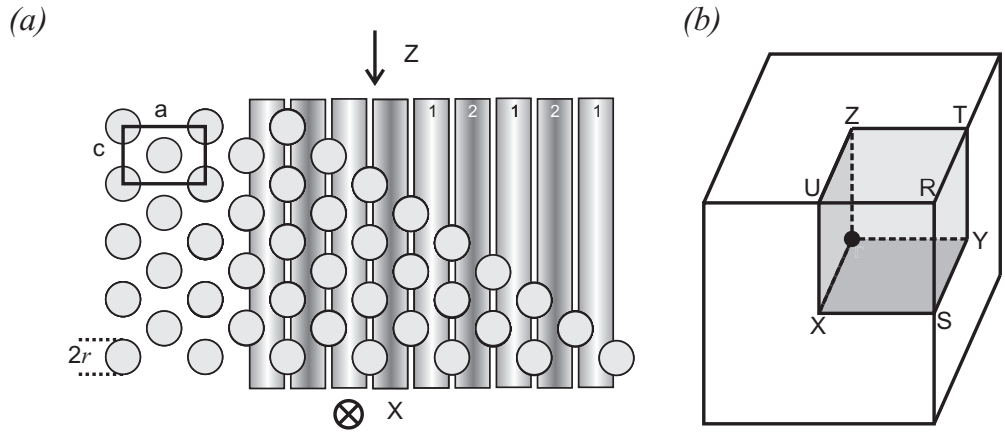


**Figure 5.1:** Schematic representation of a fraction of an inverse woodpile photonic crystal in real space ($a$) and reciprocal space ($b$). In ($a$) grey circles with radius $r$ represent air holes drilled in silicon. The solid rectangle marks a unit cell with lengths $a$ and $c$ of the lattice of a two-dimensional crystal. The centers of the perpendicular cylinders are aligned exactly between columns of cylinders of the other set. Each set of cylinders forms an identical two-dimensional lattice. In ($b$) the irreducible Brillouin zone of a simple orthorhombic lattice is illustrated (grey cube). $\Gamma, R, S, T, U, X, Y$ and $Z$ mark points of high symmetry on the lattice.

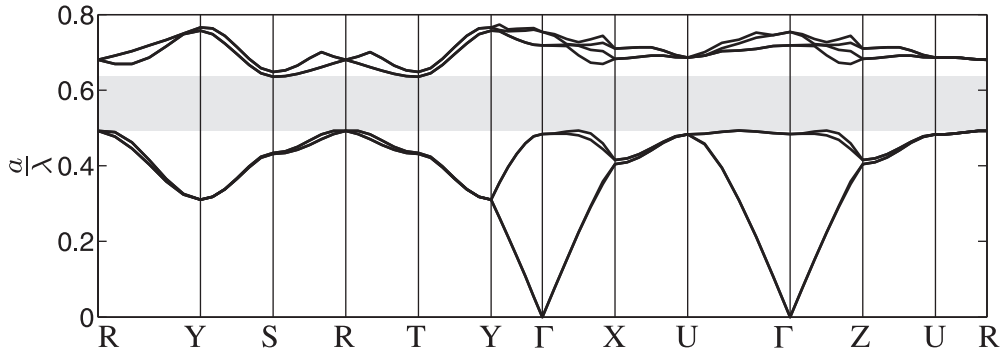


**Figure 5.2:** Calculated dispersion relations (solid lines) for the first eight optical modes in an inverse woodpile photonic crystal made of air holes in silicon of infinite size ($\frac{r}{a} = 0.24$, $\epsilon_{air} = 1$ and $\epsilon_{Si} = 12.1$, calculated with the MIT Photonic Bandgap Package). The grey area marks the photonic band gap.

This volume is $\frac{1}{8}$ of the volume of the marked unit cell in reciprocal space. The reflectivity is measured along the $\Gamma X$-direction and $\Gamma Z$-direction. The $\Gamma X$-direction is parallel with the second set of etched pores and parallel to the $\Gamma K$-direction of the surrounding two-dimensional photonic crystal. The $\Gamma Z$-direction is parallel with the first set of etched pores forming the two-dimensional photonic crystal. A schematic representation of the crystal is presented in Fig. 3.2 and Fig. 3.3.

### 5.1.1 Dispersion relation

Fig. 5.2 shows calculated dispersion relations for optical modes in a silicon inverse woodpile crystal with $\frac{r}{a} = 0.24$. Between $\frac{a}{\lambda} = 0.493$ and $\frac{a}{\lambda} = 0.636$ a broad three-dimensional photonic band gap is formed of 25.1% relative width. The bandstructure in both the $\Gamma X$- and $\Gamma Z$-direction is identical and shows two stopgaps. The lowest frequency stopgap is

between $\frac{a}{\lambda} = 0.401$ and $\frac{a}{\lambda} = 0.416$, which is closed in the $XU$-direction. In the experiment a NA = 0.65 objective is used, resulting in an angle-averaged spectrum, reducing the appearance of this stopgap. The second stopgap between $\frac{a}{\lambda} = 0.493$ and $\frac{a}{\lambda} = 0.670$ is part of the band gap, and the red frequency edge of the stopgap coincides with the edge of the band gap.

Deviations from the ideal crystal geometry are described by [15, 16]. They consider deviations from $a = \sqrt{2}c$, deviations from $\frac{r}{a}$, different $r$ for both sets, angular misalignments of the air cylinders, tapering of the air pores and deviations from the lateral alignment of the sets of air pores. The band gap of this kind of structure is robust to these types of deviations.

## 5.2 Results

### 5.2.1 Reflectivity in the $\Gamma X$- and $\Gamma Z$-direction

For an inverse woodpile crystal, the symmetry of the lattice is the same when measured parallel with the $\Gamma X$- or $\Gamma Z$-direction and therefore one expects the same reflectivity if the surface of the crystal is identical for both directions. Therefore, experimental differences reveal differences in the two etch directions. In this section, we compare the reflectivity

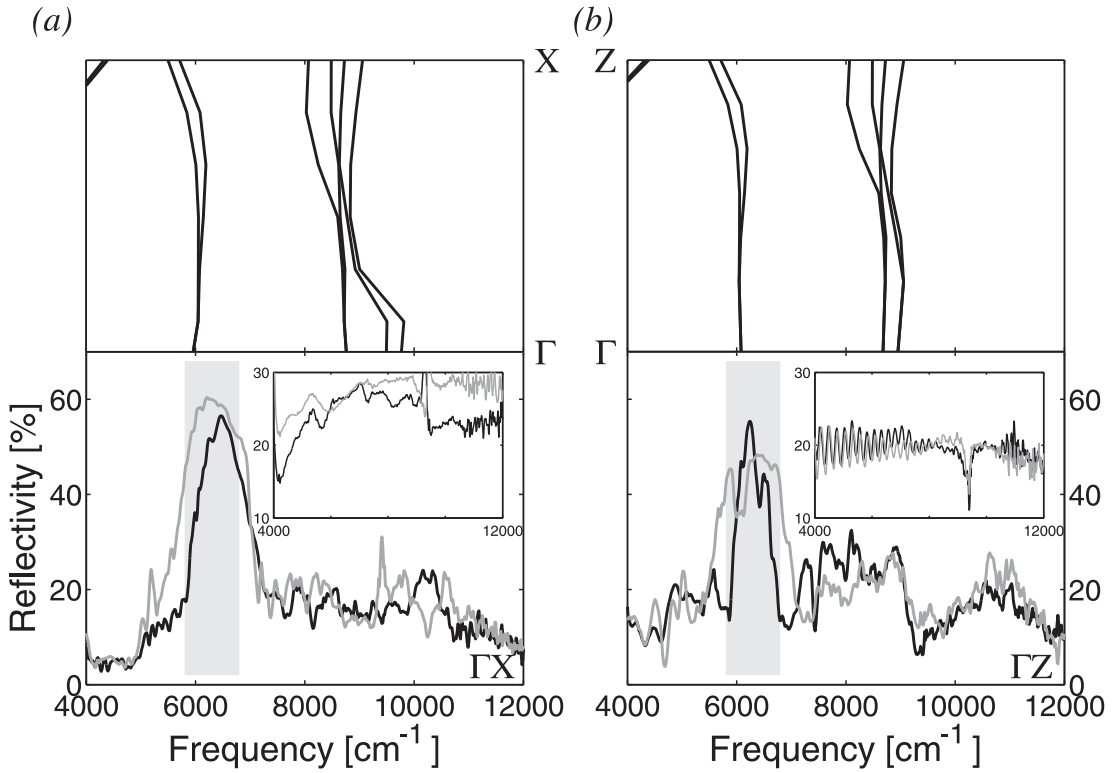


**Figure 5.3:** Comparison between calculated dispersion relations and measured reflectivity for $\perp$-(black) and $\parallel$-(grey) polarized waves in the $\Gamma X$- ($a$) and $\Gamma Z$-direction ($b$) for an inverse woodpile photonic crystal with $r = (145 \pm 9)$ nm. Spectra of non-photonic references shown in the insets are obtained on silicon ($a$) and on top of a two-dimensional crystal ($b$), measured parallel with the pores. The grey areas between 5800 and 6800 cm$^{-1}$ mark the overlap frequencies of the observed peaks in both the $\Gamma X$- and $\Gamma Z$-direction.

acquired for both directions for the best-aligned crystal based on SEM pictures, see Fig. 3.4. The reflectivity was measured for two orthogonal polarizations, where we use the perpendicular pores as reference. The incident wave is $\perp$-polarized when the polarization is perpendicular to these pores, the incident wave is $\parallel$-polarized when the polarization is parallel to these pores. For two-dimensional crystals it is known that plane waves with a certain polarization cannot couple to all modes, depending on the symmetry of the crystal [26]. We do not yet have predictions for the inverse woodpile crystal if certain modes can only couple to specific polarizations.

Fig. 5.3 shows a comparison between calculated dispersion relations and measured spectra for $\perp$-(black) and $\parallel$-(grey) polarized waves in the $\Gamma X$- ($a$) and $\Gamma Z$-direction ($b$) for a crystal with $r = (145 \pm 9)$ nm. A broad reflectivity peak appears for both directions and polarizations with maxima up to 60% that overlap between 5800 and 6800 cm$^{-1}$ (grey area). The reflectivity was measured at several locations on the crystal to confirm the reproducibility, see Sec. 5.2.3. The non-photonic references shown in the insets are collected on the silicon near the structure for the $\Gamma X$-direction and on top of a two-dimensional crystal for the $\Gamma Z$-direction, see black dashed circles in Fig. 3.3. The reference surface for the $\Gamma X$-direction is likely affected by the fabrication steps. The reference measurement for the $\Gamma X$-direction contains fringes, which are caused by internal reflections inside the two-dimensional crystal. This is explained in Sec. 5.2.3. The reference spectra are clearly different from the reflectivity of the photonic crystals.

The dispersion relation is calculated for an infinite inverse woodpile photonic crystal with pore radii of $\frac{r}{a} = 0.211$. Although small deviations like the relative alignment of the pore sets have not been included in the calculations, this bandstructure can be used for a comparison with the measured data to explain the main features of the reflectivity. The calculation describes the eight optical modes with lowest eigenfrequencies. The small differences in the calculated bandstructure for both directions are numerical.

A second order stopgap is predicted between 6190 and 8026 cm$^{-1}$, which is part of the predicted band gap between 6190 and 7640 cm$^{-1}$. A major reflectivity peak is observed for both directions and polarizations near the predicted band gap, with an overlap region between 5800 and 6800 cm$^{-1}$, corresponding to a relative stopgap width of $(15 \pm 1)$%. From calculations, this structure should have a relative band gap width of 21%. The peak for $\parallel$-polarized waves is broader than for $\perp$-polarized waves in both directions. For the $\Gamma Z$-direction, several troughs appear in the spectra. These are likely caused by contaminations, since for other samples the peaks appear as smooth as for the $\Gamma X$-direction. The reflectivity peaks appear at a slightly lower frequency than the expected band gap. The reason for this is unknown, but it is likely caused by the inaccuracies in $a$, $c$ and $r$ and small alignment deviations that were not included in the calculations. The overlapping peaks for both directions and polarizations are an indication of a photonic band gap and is explicitly shown in Fig 5.4.

Below 5000 cm$^{-1}$, the reflectivity behaves similarly for $\perp$- and $\parallel$- polarized waves for a specific crystal orientation. When the spectra are compared for a specific polarization but different crystal orientation, the reflectivity behaves differently. This difference is caused by the surrounding medium of the crystal. For the $\Gamma X$-direction ($a$), the medium behind the crystal is a two-dimensional photonic crystal, which behaves as medium with a constant effective refractive index that is slightly higher than for the inverse woodpile crystal, since the silicon filling fraction of a two-dimensional crystal is larger. For the $\Gamma Z$-direction the medium behind the crystal is silicon. This strong refractive index contrast results into internal reflections inside the crystal between the air and silicon interfaces,

appearing as a Fabry-Perot fringe pattern in the reflectivity. The fringes are also present on the non-photonic references. The higher average reflectivity for the $\Gamma Z$-direction is also caused by the different surrounding media.

The calculated dispersion relations predict a first order stopgap between 4387 and 5497 $cm^{-1}$. This stopgap does not correspond to a major reflectivity peak. Nevertheless, an increased average reflectivity in this frequency range is observed for both polarizations. This stopgap is not apparent in the spectra since the spectrum is averaged over multiple angles. For frequencies above 8000 $cm^{-1}$ the reflectivity can not be interpreted, and more bands need to be calculated.

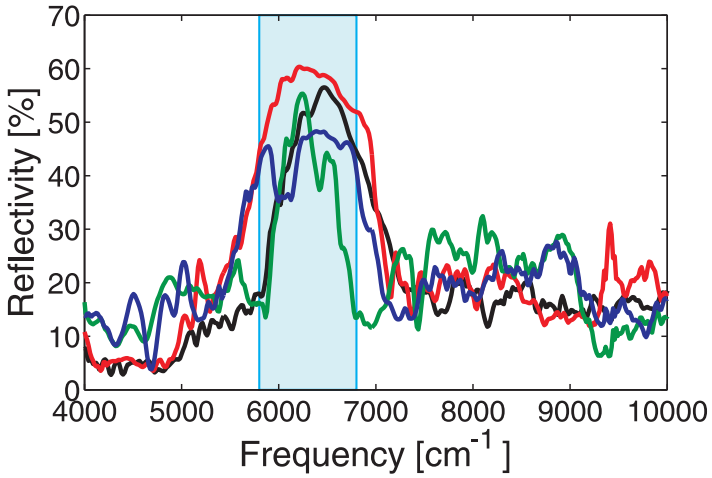


**Figure 5.4:** (*color*) Same reflectivity spectra as displayed in Fig. 5.3. The black curve is the reflectivity for $\perp$-polarized light in the $\Gamma X$-direction. The red curve is the reflectivity for $\parallel$-polarized light in the $\Gamma X$-direction. The green curve is the reflectivity for $\perp$-polarized light in the $\Gamma Z$-direction. The blue curve is the reflectivity for $\parallel$-polarized light in the $\Gamma Z$-direction. The blue area between 5800 and 6800 $cm^{-1}$ marks the overlap frequencies of the observed peaks.

### 5.2.2 Reflectivity for different samples

Each sample contains up till 8 inverse woodpile crystals, see Sec 3.1. Each crystal was fabricated independently using the same mask and etching procedures, resulting in identical crystals except for deviations caused by the relative lateral alignment of the sets of pores.

For each clean crystal, reflectivity for $\perp$- and $\parallel$-polarized waves have been measured for both directions. The bottom panels in Fig. 5.5 give an overview of the frequency and halfwidth of the highest reflectivity peaks close to the expected band gap, measured for three samples with different pore radii. The corresponding maximum reflectivity and average background reflectivity are shown in the top panels. We have selected for each direction and polarization one spectrum that is representative for the crystal. This overview was used to identify crystals with overlapping reflectivity peaks for all directions and polarizations, which is a signature of a photonic band gap.

The maximum reflectivity measured on a photonic crystal is 60%, independent of the polarization and direction. This was observed for different samples for uncontaminated well-polished surfaces, see crystal 5 in ($a$), crystals 3, 4, and 7 in ($b$), and crystal 2 in ($c$). This is about 20% higher than reported by Schilling et al. [51]. We agree with the

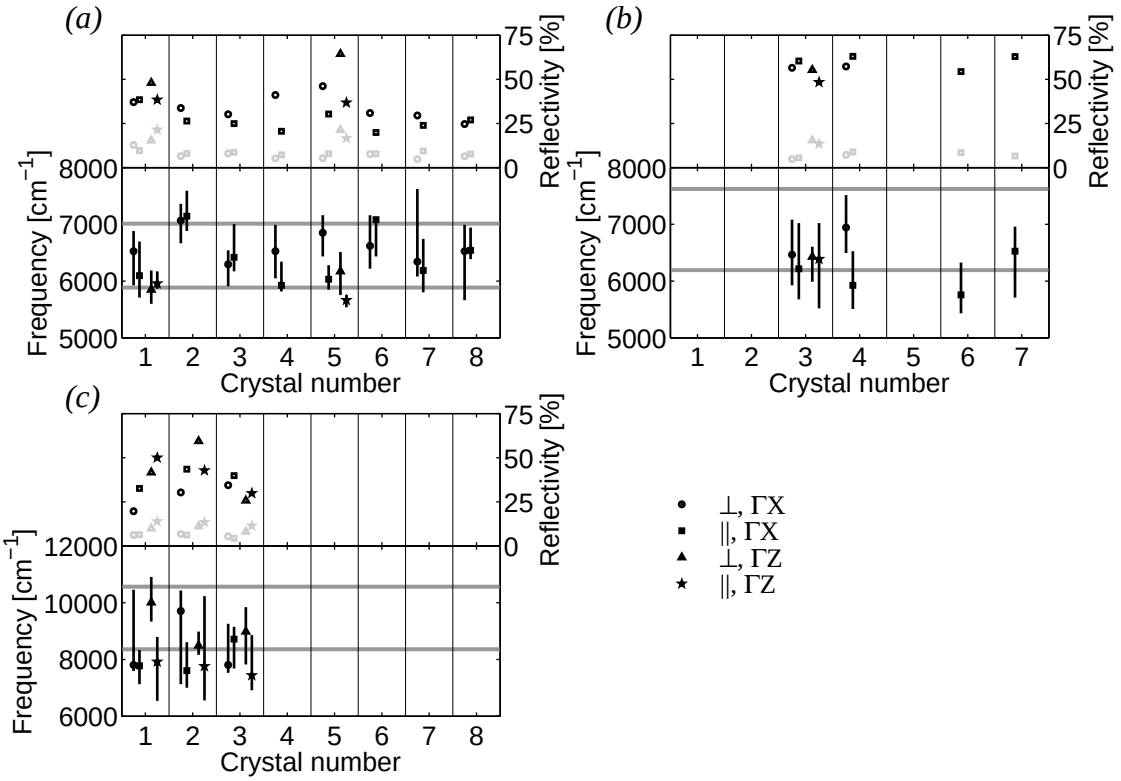


**Figure 5.5:** Overview of the major reflectivity peaks for three samples with different pore radii; $r = (136 \pm 7)$ nm $(a)$, $r = (145 \pm 9)$ nm $(b)$ and $r = (181 \pm 11)$ nm $(c)$. Circles are measurements obtained from $\perp$-polarized waves in the $\Gamma X$-direction, squares from $\parallel$-polarized waves in the $\Gamma X$-direction, triangles from $\perp$-polarized waves in the $\Gamma Z$-direction and stars from $\parallel$-polarized waves in the $\Gamma Z$-direction. Bottom panels show peak frequencies (symbols) with corresponding half widths (bars) and edges of the calculated band gaps (grey). Top panels show maximum reflectivity (black) and average background reflectivity between 4500 and 5000 cm$^{-1}$ (grey) of the spectra used in the bottom panels.

proposition that the reflectivity does not reach 100% due to a slight surface roughness or the roughness at the pore walls leading to scattering losses.

The average background reflectivity between 4500 and 5000 cm$^{-1}$ is lower for the $\Gamma X$-direction than for the $\Gamma Z$-direction, which is caused by the different medium behind the crystal. The background reflectivity decreases with increasing pore radius, since the silicon filling fraction is reduced.

Fig. 5.5$(a)$ shows the overview of the reflectivity peaks for sample Ad2b-14112008 with $r = (136 \pm 7)$ nm. All crystals show overlapping reflectivity peaks in the $\Gamma X$-direction close to the calculated band gap. From SEM pictures, the alignment of crystal 1 is best. However, there is an angular misalignment of the second set of pores; the pores are drilled approximately $7^o$ off from the ideal etch direction in the $yz$-plane of Fig. 3.3 for all crystals. Nevertheless, this crystal shows for both polarizations and directions overlapping peaks. Except for crystal 2, the reflectivity peaks for all crystals are in the same frequency region as for crystal 1, demonstrating the reproducibility of our fabrication method. Especially crystal 1 and crystal 5 show high reflectivity maxima.

Fig. 5.5$(b)$ shows the overview for sample Ad3b-14112008 with $r = (145 \pm 9)$ nm. Based on SEM pictures, crystal 3 is the best crystal from all samples, see Fig. 3.4.

High reflectivity and overlapping reflectivity peaks are observed for both directions and polarizations, making it an excellent candidate for a photonic band gap. This crystal was used in Fig. 5.3. Crystal 4 has a larger lateral deviation from the ideal crystal, resulting in non-overlapping reflectivity peaks. The SEM picture of crystal 6 looks similar to the SEM picture of crystal 4 resulting in a comparable reflectivity peak and average background reflectivity. Crystal 7 looks as good as crystal 3, resulting in a comparable peak width and average background reflectivity.

Fig. 5.5($c$) shows the overview for sample Ad2a-29092008 with $r = (181 \pm 11)$ nm. Based on SEM pictures, crystal 2 is the best crystal. Indeed, both crystal 2 and 3 demonstrate overlapping reflectivity peaks for both directions and polarizations, which makes them promising candidates for a photonic band gap and future emission experiments.

It is remarkable how well the location of the reflectivity peaks agrees with the calculated bandstructure for the ideal crystal. This overview shows the advantage of our fabrication method; we have several crystals on one sample and based on reflectivity measurements we can select possible candidates for a band gap. This indicates that our fabrication method gives reproducible crystals. This also supports the predictions that the band gap of the inverse woodpile structure is robust to deviations [15, 16].

### 5.2.3 Surface scans over inverse woodpile photonic crystals

Inverse woodpile crystals have been characterized by measuring the reflectivity in the center of the crystal surface. Acquiring reflectivity at several positions on the surface gives information about reproducibility of the measurements and how crystal boundaries affect spectra. This section describes examples of position controlled reflectivity measurements on inverse woodpile crystals. We show scans for the crystal studied in Fig. 5.3.

**Y-scan $\perp$-polarization** Figure 5.6 shows a Y-scan for $\perp$-polarized light over an inverse woodpile crystal. The scan was started on the surrounding two-dimensional crystal, continued over the inverse woodpile crystal and ended on the two-dimensional crystal. A reflectivity maximum of 70% is observed on the two-dimensional crystal corresponding to the $\Gamma K$ stopgap between 4700 and 6300 cm$^{-1}$. A higher frequency peak starts at 9000 cm$^{-1}$, belonging to the higher order stopgap. A spectrum is plotted in ($c$) at $y = 0.42$ $\mu$m. The difference in the spectra for the two-dimensional crystal between $y < 6$ $\mu$m and $y > 14$ $\mu$m is caused by the surface of the crystal.

At the interface between the two-dimensional and inverse woodpile crystal ($y = 6$ and 14 $\mu$m), the first reflectivity maximum decreases in amplitude and broadens. Measurements on other crystals indicate that the $\Gamma K$-reflectivity maximum does not split, as might be inferred from ($a$), but a new frequency peak appears at the red side of the broadened $\Gamma K$-peak, which is only present at this interface. This low frequency peak disappears when the focus is moved to the center of the inverse woodpile crystal. The main peak forms a 60% reflectivity peak between 5800 and 6800 cm$^{-1}$, which is close to the amplitude of the $\Gamma K$-peak on the two-dimensional crystal, as has been observed for all well-aligned crystals. The frequency range is somewhat lower than the predicted band gap. There is a small peak at the red side of the major peak, which is caused by the lowest frequency stopgap, see Fig. 5.3. The silicon filling fraction is smaller for inverse woodpile crystals than for two-dimensional crystals, which results in a lower refractive index in the long-wavelength limit and thus a lower reflectivity. From this scan we conclude that there is a strong difference between the reflectivity of the two-dimensional crystal and the

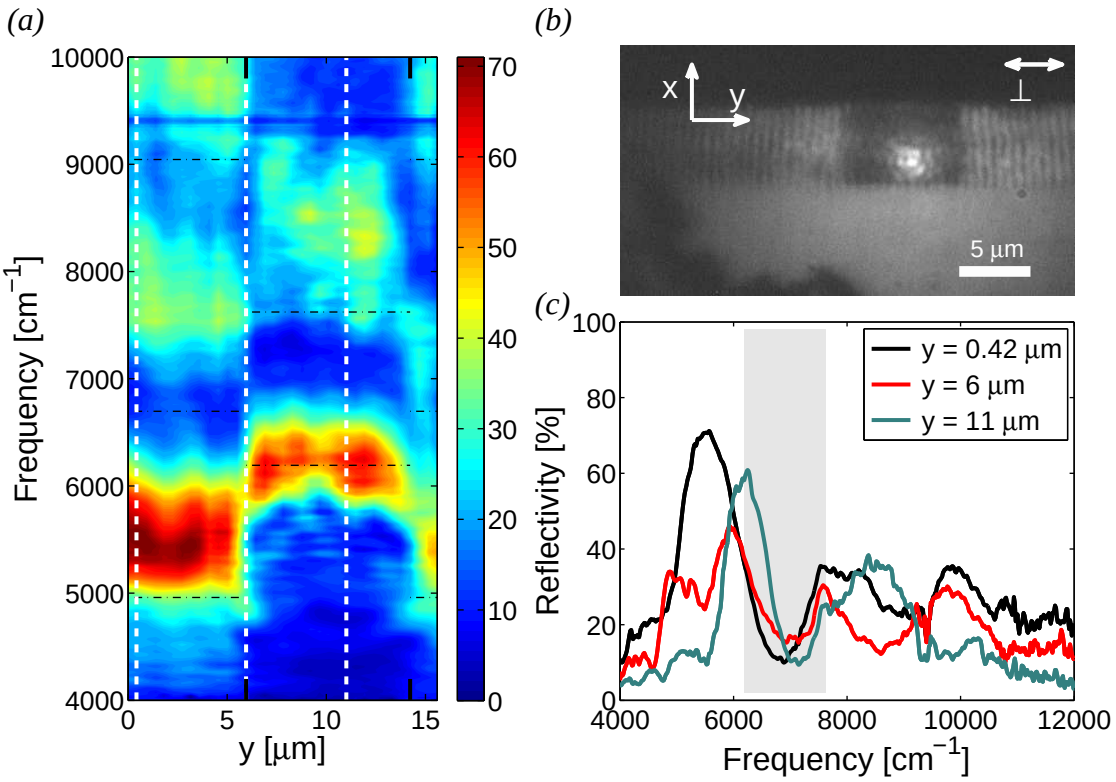


**Figure 5.6:** *(color)* Y-scan over a crystal for ⊥-polarization, measured parallel with the $\Gamma X$-direction. The scan started on the surrounding two-dimensional crystal ($y = 0$ $\mu$m), continued over the inverse woodpile crystal ($6 < y < 14$ $\mu$m) and ended on the two-dimensional crystal, where the sample was moved with steps of $(0.46 \pm 0.05)$ $\mu$m. (*a*) Collected spectra for several y-positions. The black lines on the horizontal axis indicate the boundaries of the crystal. The white dashed lines are spectra displayed in (*c*). The black dash-dotted lines indicate the calculated edges of the stopgaps in the $\Gamma K$-direction for two-dimensional crystals and band gaps for inverse woodpile crystals. (*b*) Microscope picture of the crystal. (*c*) Three reflectivity spectra measured at the y-coordinates given by the white dashed lines in (*a*) and the calculated band gap (grey).

inverse woodpile crystal. The reflectivity on the three-dimensional crystal is constant on the crystal surface, except near the boundaries.

**Y-scan ∥-polarization** Figure 5.7 shows a Y-scan for ∥-polarized light over the same crystal as in Fig. 5.6. On the surrounding two-dimensional crystal a reflectivity peak of 60% is observerd, corresponding to diffraction near the $K$-point. A higher order reflectivity peak is observed between 5800 and 7500 cm$^{-1}$, most likely belonging to simple Bragg diffraction or bad coupling to modes inside the structure. A spectrum is plotted in (*c*) at $y = 0.13$ $\mu$m.

At the boundary between the two-dimensional and inverse woodpile crystal ($y = 6$, 14 $\mu$m), the $\Gamma K$-reflectivity peak decreases in amplitude and broadens. Measurements on other crystals indicate that the $\Gamma K$-peak blue-shifts and broadens to the broad reflectivity maximum between 5800 and 7800 cm$^{-1}$, which is close to the amplitude of the original peak on the two-dimensional crystal. This frequency range corresponds with the predicted band gap, but is broader than for the scan in Fig. 5.6. An overlapping reflectivity peak is visible at the red side of the major peak, which might be caused by the lowest frequency

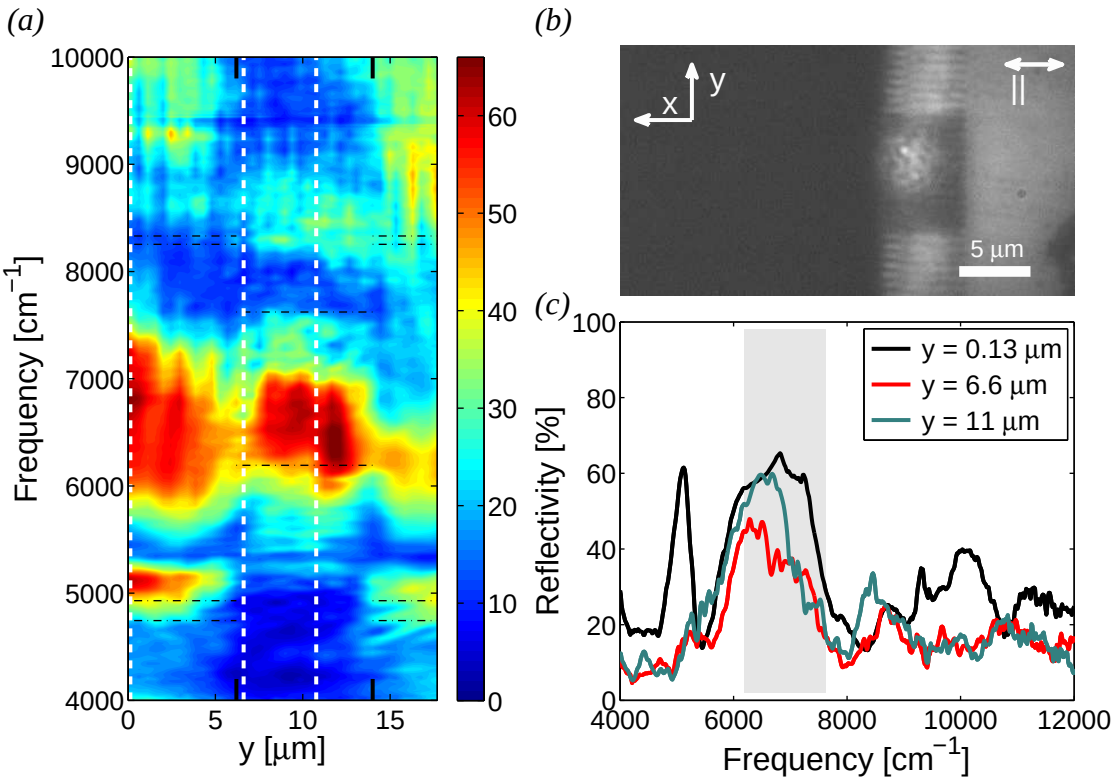


**Figure 5.7:** *(color)* Y-scan over the same crystal as in 5.6 for ∥-polarization, measured parallel with the $\Gamma X$-direction. The scan started on the surrounding two-dimensional crystal ($y = 0$ $\mu$m), continued over the inverse woodpile crystal ($6 < y < 14$ $\mu$m) and ended on the two-dimensional crystal, and the sample was moved with steps of $(0.46 \pm 0.05)$ $\mu$m. (*a*) Collected spectra for several y-positions. The black lines on the horizontal axis indicate the boundaries of the crystal. The white dashed lines are spectra displayed in (*c*). The black dash-dotted lines indicate the calculated edges of the stopgaps in the $\Gamma K$-direction for two-dimensional crystals and band gaps for inverse woodpile crystals. (*b*) Microscope picture of the crystal. (*c*) Three reflectivity spectra measured at the y-coordinates given by the white dashed lines in (*a*) and the calculated band gap (grey).

stopgap in Fig. 5.3. For this crystal the major reflectivity peak for ∥-polarized waves is broader than for ⊥-polarized waves, which is also the case for the $\Gamma Z$-direction. The reflectivity in the long-wavelength limit is again lower for the inverse woodpile crystal than for the two-dimensional crystal, because the silicon filling fraction is smaller for inverse woodpile crystals than for two-dimensional crystals. From this scan we conclude that there is a strong difference between the reflectivity of the two-dimensional crystal and the inverse woodpile crystal. The reflectivity on the three-dimensional crystal is constant on the crystal surface, except near the boundaries. This scan and the previous scan demonstrate that this inverse woodpile crystal is indeed of excellent quality.

**Y-scan ∥-polarization in the $\Gamma Z$-direction** Fig. 5.8 shows a Y-scan for a different crystal in the $\Gamma Z$-direction for ∥-polarized waves (crystal 2 in Fig. 5.5(*c*)). On the surrounding two-dimensional crystal no reflectivity peak is visible since the crystal is probed parallel with the pores. On the inverse woodpile crystal diffraction peaks appear. Fringes are present in the spectra for both types of crystals due to internal reflections. The fringe spacing increases for the inverse woodpile crystal since the silicon filling fraction $\Phi$ is

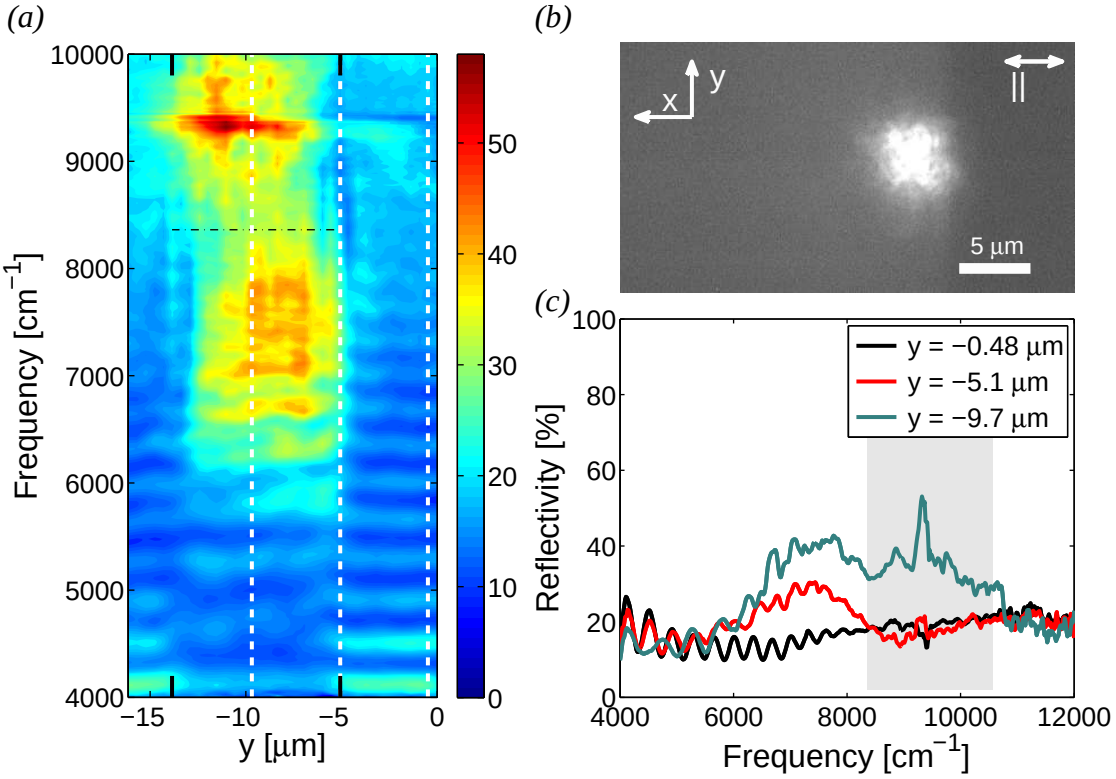


**Figure 5.8:** *(color)* Y-scan over a crystal with $r = (181 \pm 11)$ nm for ∥-polarization, measured parallel with the $\Gamma Z$-direction. The scan started on the surrounding two-dimensional crystal ($y = 0$ $\mu$m), continued over the inverse woodpile crystal ($-14 < y < -5$ $\mu$m) and ended on the two-dimensional crystal, where the sample was moved with steps of $(0.46 \pm 0.05)$ $\mu$m. (*a*) Collected spectra for several y-positions. The black lines on the horizontal axis indicate the boundaries of the crystal. The white dashed lines are spectra displayed in (*c*). The black dash-dotted lines indicate the calculated edges of the band gap for the inverse woodpile crystal. (*b*) Microscope picture of the crystal. (*c*) Three reflectivity spectra measured at the y-coordinates given by the white dashed lines in (*a*) and the calculated band gap (grey).

smaller for inverse woodpile crystals than for two-dimensional crystals, which results in a lower effective refractive index in the long-wavelength limit. Also for other crystals, a fringe pattern is observed on the red side of the major reflectivity peaks. For this crystal we expect from the calculated dispersion relation that the refractive index is constant below 5000 cm$^{-1}$. The fringes can be modelled with a Fabry-Perot interferometer consisting of air, photonic crystal and silicon. The spacing between the fringes can be used to estimate $\Phi$. The frequency period for the fringes $\nu_{\text{fsr}}$ between 4000 and 5000 cm$^{-1}$ for the two-dimensional crystal is $(406 \pm 16)$ cm$^{-1}$ and for the inverse woodpile crystal $(601 \pm 32)$ cm$^{-1}$. For a Fabry-Perot interferometer, the frequency range between the fringes is given by:

$$\nu_{\text{fsr}} = \frac{c_0 \cos(\theta)}{2 n_{\text{eff}} l}, \tag{5.1}$$

where $c_0$ is the speed of light in vacuum, $\theta$ is the angle of incidence, $n_{\text{eff}}$ the effective refractive index in the crystal and $l$ the width of the crystal. The refractive index can be approximated by a volume-average of the dielectric media that depends on $\Phi$:

$$n_{\text{eff}} = \sqrt{(\Phi \cdot \epsilon_{\text{Si}}) + (1 - \Phi) \cdot \epsilon_{\text{air}}} \tag{5.2}$$

We have determined from SEM pictures $r = (181 \pm 11)$ nm, $a = (697 \pm 15)$ nm, $c = (480 \pm 10)$ nm and $l = (5794 \pm 141)$ nm. Assuming that the fringes are only detected for waves close to $\theta = 0$, we can estimate $\Phi$ for both the two-dimensional crystal and inverse woodpile crystal. This results for the two-dimensional crystal in $\Phi = (0.32 \pm 0.05)$ which agrees with the calculated filling fraction of $0.38 \pm 0.10$. For the inverse woodpile crystal we find $\Phi = (0.09 \pm 0.03)$, which is in reasonable agreement with the calculated filling fraction of 0.14 calculated with the MIT photonic bandgap package where errors in $r, a, c$ have been ignored. This fringe pattern results in similar estimations for the filling fraction for the other polarization. Our model assumed paraxial propagation in a non-dispersive medium. This method becomes more accurate when a low NA objective is used, combined with light detection for longer wavelengths. We conclude that these fringes give a reasonable estimation of the filling fraction.

## 5.3 Conclusions

Polarization resolved reflectivity of inverse woodpile photonic crystals has been studied for a range of pore radii. Several crystals show overlapping reflectivity maxima for both $\perp$- and $\parallel$-polarized waves. We have presented the reflectivity of a specific crystal that seems well aligned on SEM pictures. For both polarizations in the $\Gamma X$- and $\Gamma Z$-direction, an overlapping reflectivity peak is observed between 5800 and 6800 cm$^{-1}$, which is a (strong) indication of the presence of a band gap. It will be exciting to confirm this *forbidden zone* with spontaneous emission measurements.

The reflectivity obtained for several crystals in the $\Gamma X$- and $\Gamma Z$-direction show qualitatively similar spectra. The reflectivity in the $\Gamma Z$-direction contains fringes caused by internal reflections in the crystals. These fringes were used to estimate the silicon filling fraction of one crystal based on a simple Fabry-Perot interferometer. The obtained filling fraction agrees well with the filling fraction estimated from SEM pictures.

An overview has been made of the reflectivity peaks for all crystals and compared with calculated bandstructures. It is remarkable how well the location of the reflectivity peaks agrees with the calculated bandstructure for the ideal crystal. This overview shows the advantage of our fabrication method; we have several crystals on one sample and based on reflectivity measurements we can select possible candidates for a band gap. The results indicate that our fabrication method gives reproducible crystals. This also supports the claim that the band gap of the inverse woodpile structure is robust to deviations.

We have measured broad peaks with high reflectivities up to 60% for clean crystals. This is the highest reported reflectivity for inverse woodpile crystals designed for near-infrared frequencies.

We have studied the position-dependent reflectivity of these crystals. Except for spectra obtained near the boundaries of crystals, the reflectivity is constant. There is a clear difference between the reflectivity for the inverse woodpile crystal and the reflectivity of the surrounding media. The crystals that are likely to have a band gap, have been completely characterized this way.

# Chapter 6

# Spontaneous emission in silicon two-dimensional photonic crystals

In chapter 4 we have demonstrated by reflectivity measurements that the dispersion relation of light is strongly modified with silicon two-dimensional photonic crystals. The spectra indicate the presence of a two-dimensional band gap for TE-polarized light. Therefore, we have started experiments to investigate how spontaneous emission is modified inside such a crystal.

This experiment is also important for upcoming experiments with emission inside three-dimensional inverse woodpile crystals. Since inverse woodpile crystals are surrounded by and fabricated out of two-dimensional photonic crystals, these are excellent crystals to develop a generalized measurement procedure.

To our knowledge, no experiments have been performed inside two-dimensional photonic crystals with a similar configuration as the crystals we use, see Sec. 3.1. A few emission experiments have been performed on two-dimensional crystals slabs. In contrast with our structure, the pores in a photonic crystal slab are typically in the order of a few 100 nm deep and light is guided inside the slab. Inhibition, enhancement and redistribution of spontaneous emission for crystal slabs have been reported [33, 34].

We have experimentally studied the polarization resolved emission spectrum of lead sulphide (PbS) quantum dots in two-dimensional photonic crystals at near-infrared frequencies at room temperature. We use a novel method where the crystal is submerged in a PbS quantum dot suspension, keeping the quantum dots stable for months.

## 6.1 Experimental parameters

To study modified emission at near-infrared frequencies compatible with silicon photonic crystals, we have chosen to use semiconductor quantum dots [45]. Quantum dots are nanocrystals for which a discrete energy spectrum exists due to confinement of the electron wavefunctions. The emission can be tuned by changing the size of the dots. We have prepared a suspension of Evidot-1500 PbS quantum dots in toluene. The low concentration of $4 \cdot 10^{-7}$ M is chosen to prevent non-radiative energy transfer between the quantum dots.

A two-dimensional photonic crystal with $r = (155 \pm 8)$ nm, which has been characterized with reflectivity measurements (see Fig. 4.4), was pressed against the inner wall of a glass cuvet using a stainless steel spring. The cuvet was filled with the quantum dot suspension, see Fig. 6.1. The great advantage of keeping the quantum dots in toluene is

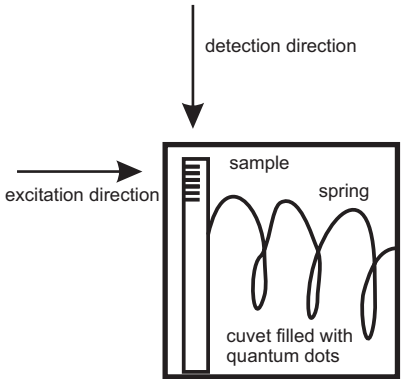


**Figure 6.1:** Schematic representation of the sample in the set-up.

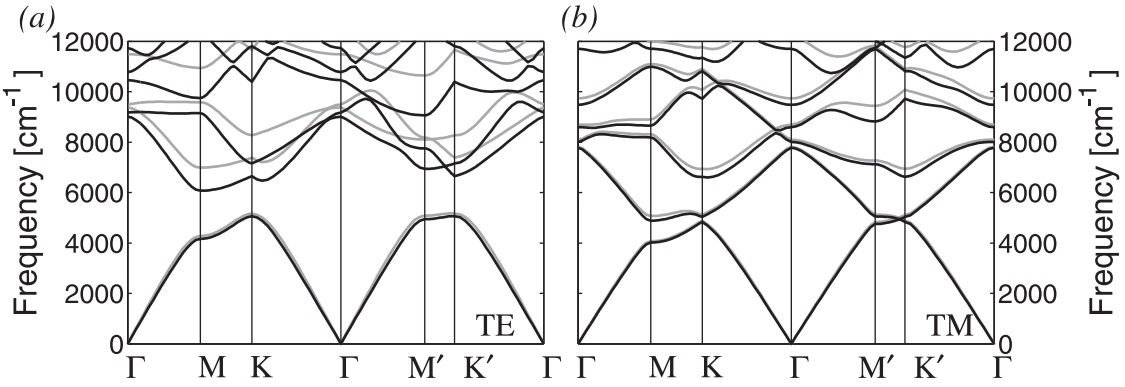


**Figure 6.2:** Calculated dispersion relations (solid lines) for optical modes in an infinite two-dimensional photonic crystal with a centred rectangular lattice made of air holes in silicon ($a$ = 690.6 nm, $c$ = 486.3 nm, $r$ = 155 nm, $\epsilon_{\text{toluene}} = 2.19$ and $\epsilon_{Si} = 12.25$, calculated with the MIT Photonic Bandgap Package). Dispersion relations for TE ($a$) and TM ($b$) polarized waves have been calculated with unfilled pores (grey) and pores filled with toluene (black).

that they remain stable for months since effects like photo-oxidation are prevented [45]. For comparison, PbS quantum dots inside a nitrogen chamber only, as studied before by Nikolaev et al. [28], remain stable for a day. Therefore, using stable suspensions allows the study of delicate silicon photonic crystals. A disadvantage is that emitters are not only located inside the crystal, but also surround the entire structure, causing background signal.

The toluene decreases the refractive index contrast inside the photonic crystal, reducing the photonic strength and modifying the dispersion relation, see Fig. 6.2. The two-dimensional band gap for TE-polarized light shifts to 5057 and 6070 cm$^{-1}$. The dispersion relation for TM-polarized light hardly changes for lower frequency bands. Higher frequency bands are shifted towards lower frequencies. In our experiment we can detect emission between 6300 and 7500 cm$^{-1}$. Therefore, we cannot probe the two-dimensional band gap, but we can observe features caused by the higher bands, like enhanced spontaneous emission near the band gap edge.

A 0.05 NA objective was used to excite the quantum dots at $\lambda_{ex}$ = 633 nm with a HeNe laser[1]. The excitation objective excites the quantum dots from a direction parallel

[1]Excitation path 2 in Fig. 3.7

with the pores of the crystal. A 0.70 NA objective is aligned parallel to the $\Gamma M'$-direction to detect the emitted light. A separate excitation and detection objective minimizes the detection of quantum dots outside the photonic crystal. In previous attempts, we have used the 0.70 NA objective both for excitation and for detection[2]. These measurements indicate that mainly quantum dots between the structure and the glass wall are detected, instead of inside the pores. Therefore, we decided to use separate excitation and detection objectives.

The foci of the excitation and detection objectives were mutually aligned by maximizing the detected emission spectrum of the quantum dot suspension, where the structure was at least 1 mm away from the focus. The surface of the crystal was found to be in focus of the detection objective by directing an alignment beam through the detection objective. The surface was placed in focus when the reflected light on the silicon close to the crystal was maximal.

## 6.2 Results

Fig. 6.3 shows a comparison between a calculated dispersion relation ($a$) and measured polarization dependent emission spectra of PbS quantum dots ($b - d$). The emission spectra were obtained by scanning the detection focus over the surface. The scan was started on the silicon surrounding the crystal, continued over the crystal and finished in the quantum dot suspension (similar to the reflectivity scan in Fig. 4.6). The complete scan is displayed in Fig. 6.4. The lowest intensity was obtained when the detection focus was above silicon. The detected intensity remains approximately constant above the surface, indicating that the detected light originates mainly from quantum dots above the silicon surface. The intensity increases when the detection focus is in the photonic crystal. The intensity is maximum in the quantum dot suspension.

The shapes of the emission spectra for TE and TM polarized light detected above silicon in Fig. 6.3($b$) are almost identical to the emission spectra in the quantum dot suspension ($d$). Small deviations are related to the difference in intensity and to background subtraction. Therefore, the emission is not affected by the presence of a silicon-toluene interface. The shape of the emission spectrum significantly changes when the detection focus is in the photonic crystal ($c$). For TE polarized light, three intriguing sharp emission maxima are observed at $\nu_1 = 6833$, $\nu_2 = 6959$ and $\nu_3 = 7066$ cm$^{-1}$. We define the normalized peak difference $\Delta I$ as:

$$\Delta I = \frac{I_{\nu_i} - I_{\text{ref}}}{I_{\text{ref}}} \tag{6.1}$$

with $I_{\nu_i}$ the intensity at one of the three reflectivity peaks, and $I_{\text{ref}}$ a reference intensity. We choose for $I_{\text{ref}}$ the average intensity between 6764 and 6774 cm$^{-1}$, since the spectrum does not change in this frequency range when the detection focus is above silicon, in the photonic crystal or in the suspension. Fig. 6.4($b$) shows that the peaks only appear when the detection focus is in the photonic crystal. We conclude that these emission peaks are detected from quantum dots in the crystal.

To investigate the cause of the three peaks, we compare their frequencies (vertical dashed lines) to calculated dispersion relations in Fig. 6.3. This comparison reveals that the two highest frequency peaks $\nu_2$ and $\nu_3$ appear near special features in the bandstructures, namely a flat band at $M'$ ($\nu_2$) and a mini gap between $M'$ and $K'$ ($\nu_3$). However,

[2]Excitation path 1 in Fig. 3.7

this mini gap can also be caused by an inaccuracy of the calculated bandstructure. Nevertheless, this correspondence suggests that the peaks would correspond to van Hove singularities. Van Hove singularities are frequencies for which the LDOS shows sharp maxima, which can be expected near flat bands. This would be highly exciting, since near such singularities intricate quantum optics including unusual fractional decay has been predicted [54]. Nevertheless other possible causes for the peaks should be carefully evaluated, like redistribution of emission. Future experiments should include studies as a function of lattice parameter and time-resolved emission.

For TM polarized light the spectrum of quantum dots in the crystal is similar to the emission spectrum in the suspension, except for a small peak at 6827 $cm^{-1}$, near $\nu_1$. Again, this peak is present only when the detection focus is in the crystal. At present, the cause for this peak is unknown.

## 6.3 Conclusions

We have studied the polarization-dependent emission spectra of PbS quantum dots inside novel two-dimensional photonic crystals. We have managed to detect emission from quantum dots in the photonic crystal. We observed that the photonic crystal modifies the emission spectra for TE polarized light. Near the edge of the calculated bands, intriguing sharp peaks are observed, suggesting of van Hove singularities. Further experiments are required to investigate the cause for these peaks.

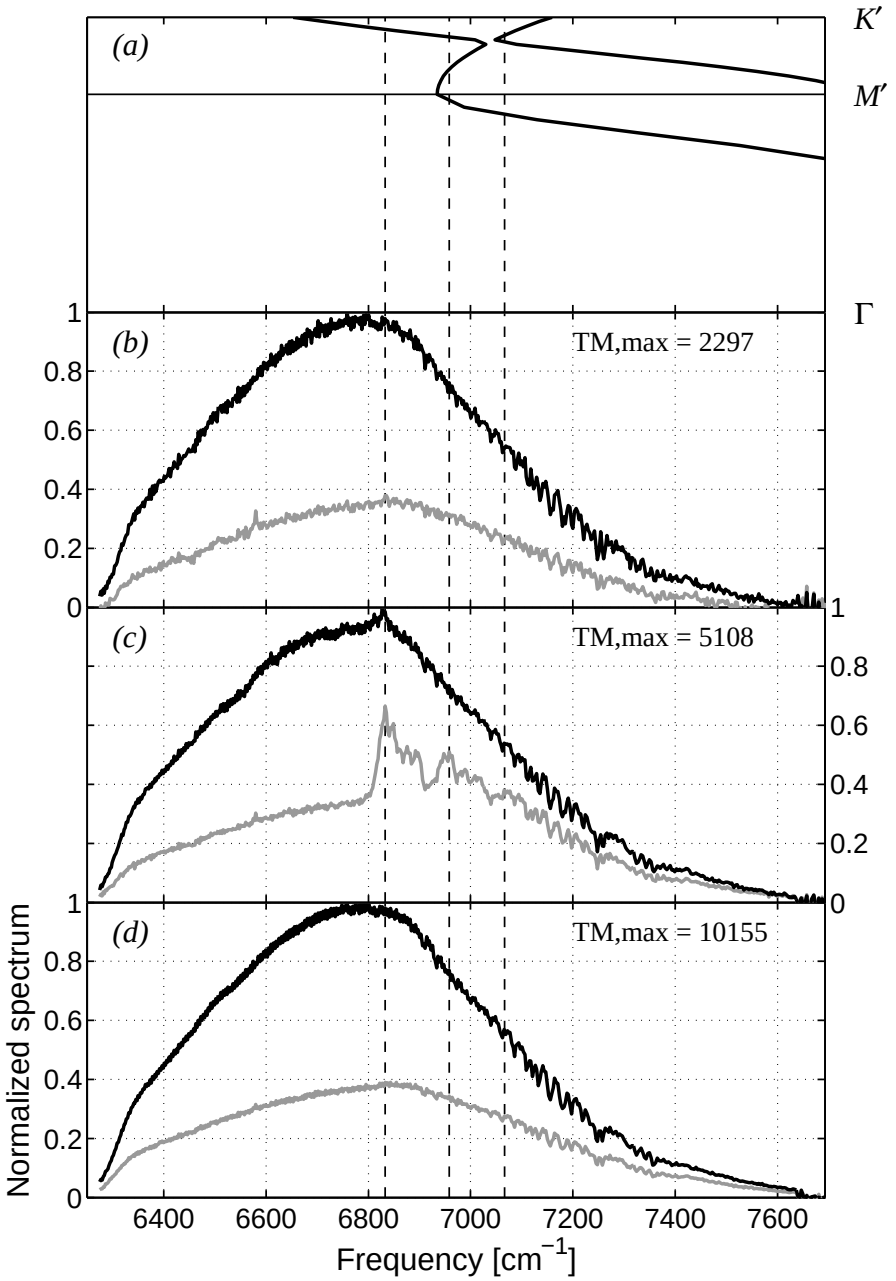


**Figure 6.3:** ($a$) Calculated dispersion relation for TE polarized light. ($b-d$) Measured emission spectra for TE (grey) and TM (black) polarized light when probed above silicon ($b$), the center of the photonic crystal ($c$) and in the quantum dot suspension ($d$). All spectra have been normalized to the maximum collected intensity for TM polarized light, which are displayed in the graphs in ADU's. The vertical dashed lines mark peak intensities at 6833, 6959 and 7066 cm$^{-1}$ observed for quantum dots in the crystal. The PbS quantum dots are excited with $\lambda = 633$ nm at 100 mW. All spectra are corrected for background light and dark counts.

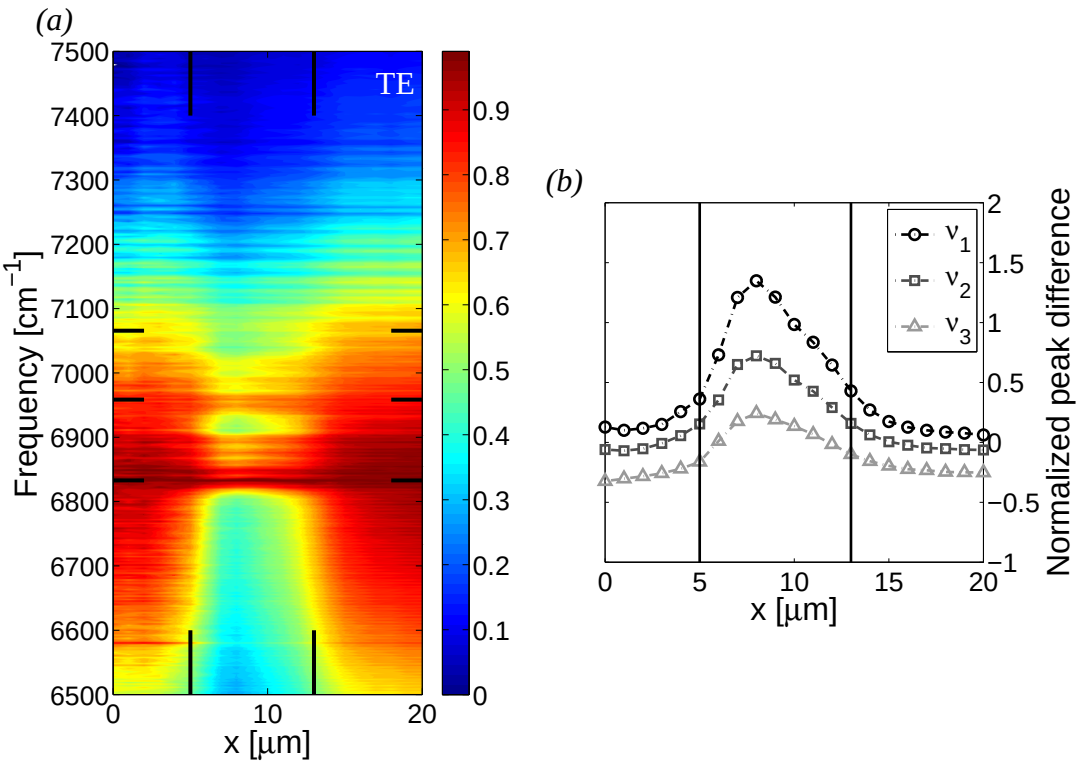


**Figure 6.4:** *(color)* (*a*) X-scan of the normalized emission spectrum over a crystal for TE polarized light, measured parallel with the $\Gamma M'$-direction. The scan started with the detection focus above the silicon ($x = 0$ $\mu$m), continued over the crystal ($6 < x < 14$ $\mu$m) and finished in the suspension, where the sample was moved with steps of $(1.0 \pm 0.1)$ $\mu$m. The emission spectrum is normalized to the maximum value of the collected TE spectrum for each position. The colorbar indicates the normalized emission spectrum. (*b*) Position-dependent normalized peak difference of intensity maxima observed in (*a*) at the black horizontal lines for $\nu_1 = 6833$, $\nu_2 = 6959$ and $\nu_3 = 7066$ cm$^{-1}$, with respect to the average intensity between 6764 and 6774 cm$^{-1}$. The difference is normalized to the average spectrum between 6764 and 6774 cm$^{-1}$. The black vertical lines in both figures mark the boundaries of the crystal, estimated from camera pictures.

# Chapter 7

# Conclusions and recommendations

We have studied light propagation and emission in novel strong-interacting two-dimensional and three-dimensional photonic crystals. The experiments were performed in the near-infrared to be compatible with the silicon backbones of the crystals.

Reflectivity of two-dimensional macroporous photonic crystals with a centred rectangular lattice ($a = \sqrt{2}c$) revealed strong reflectivity peaks up to 85%, demonstrating that the crystals are of excellent quality. The reflectivity has been measured as a function of pore radius in both the $\Gamma M'$- and $\Gamma K$-directions for TE and TM polarized light. Measurements were compared with calculated dispersion relations and estimated Bragg conditions. The reflectivity is in agreement and stopgaps have been successfully identified. For the $\Gamma K$-direction two separate diffraction peaks were observed; the lower frequency peak is caused by multiple-Bragg diffraction on the $K$-point and the higher frequency peak is caused by simple Bragg diffraction on the $B$-point. This interesting splitting is a general phenomenon for symmetries below the square lattice in two-dimensional crystals. This sub-Bragg diffraction peak is not present for the $\Gamma M'$-direction.The spectra confirm the presence of a two-dimensional band gap for TE polarized light.

We have studied the polarization dependent reflectivity in the $\Gamma X$- and $\Gamma Z$-direction of three-dimensional silicon inverse woodpile photonic crystals for varying pore radii. The measured reflectivity peaks are in reasonable agreement with calculated dispersion relations. The spectra demonstrate for several crystals overlapping diffraction peaks for different polarizations and directions, indicating the presence of a photonic band gap.

Novel emission experiments inside photonic crystals have been done by embedding a lead sulphide quantum dot suspension in a two-dimensional crystal. Emission peaks have been observed near the high-frequency edge of the expected two-dimensional band gap for TE polarized light. We thus conclude that these photonic crystals modify light emission.

It has been clearly demonstrated that the photonic crystals modify light propagation. We conclude that we have observed *forbidden zones* for light in both two-dimensional and three-dimensional photonic crystals by polarization resolved reflectivity measurements.

## 7.1 Suggestions for improvement

We have some suggestions to improve the reflectivity measurements on two-dimensional crystals. Present results have been measured with a NA = 0.65 reflecting objective, resulting in an angle-averaged spectrum. If the reflectivity can be measured with a lower NA objective, the comparison between measured diffraction peaks and calculated band-structures becomes more accurate.

Similar analysis as Rowson et al. [43, 44] may improve our analysis. They performed FDTD analysis to interpret spectra, which can also be done for this experiment. Especially the obtained spectra for TM polarized light in the $\Gamma K$-direction are not well understood based on only bandstructure calculations.

It would be interesting to cut the crystals for measurements in the $\Gamma M$-direction. This would improve the understanding of the diffraction peaks and support the observation of the two-dimensional band gap for TE polarized light.

Techniques exist to measure the dispersion relation of photonic crystals [48, 49, 50]. These techniques are based on coupling of incident light to the modes inside the structure. Resonances in the reflectivity can be used to identify this coupling and to reconstruct the bandstructure. This makes it possible to clarify whether diffraction peaks are caused by stopgaps or by other effects like a weak coupling to propagating crystal modes.

The analysis of the reflectivity measurements on inverse woodpile crystals can be improved by quantifying deviations in the alignment of the fabricated structures. This results in a more accurate comparison between theory and measured reflectivity. One could experimentally confirm how the alignment affects the stopgaps [13, 15, 16].

The reflectivity was measured in the $\Gamma X$-direction and $\Gamma Z$-direction. Probably, inverse woodpile crystals can be cut using FIB to perform measurements in other directions.

Emission experiments were started with photonic crystals embedded in a lead sulphide quantum dot suspension. The understanding of the results could be improved by calculations of the LDOS and FDTD-simulations of the redistribution of emission.

The obtained emission spectra contain not only emission from quantum dots inside the crystal, but also from quantum dots in the surrounding suspension. Better positioning of the detection focus and confocal detection would reduce the detected emission from the surrounding suspension. More detailed spatial scanning will greatly aid in identifying emission from inside the crystals compared to unwanted background.

## 7.2 Outlook

Quantum dots have been placed inside photonic crystals to study the interaction between emitters and crystals. These emission experiments can provide information about the LDOS inside photonic crystals and the redistributed of emission. It would be interesting to study both theoretically and experimentally how the LDOS behaves for crystals with different lattice parameters in order to control light emission. It would be exciting to measure fluorescence decay in the expected band gap for different sizes of inverse woodpile crystals. The manner in which the decay rate scales with the crystal size might be a way to for the first time unambiguously identify a photonic band gap [30, 31, 32].

For the two-dimensional photonic crystal two different diffraction peaks were observed in the $\Gamma K$-direction, which are the result from multiple Bragg diffraction and simple Bragg diffraction. We propose to measure the reflectivity in the $\Gamma K$-direction for two-dimensional crystals with a different ratio between the sides of the centred rectangular unit cell. This gives the opportunity to study multiple Bragg diffraction in photonic crystals [24].

Photonic crystals can be embedded in fluids to change the refractive index contrast. The reflectivity of the submerged crystal can be studied for different refractive index contrasts, to improve the analysis of the light dispersion in the crystal and devise strategies for using photonic crystals in microfluidic systems.

# Appendix A

# Quantum efficiency of PbS quantum dots

Time-resolved emission of colloidal lead sulphide (PbS) quantum dots in an environment with a controlled local density of optical states (LDOS) has been studied experimentally. Our goal was to determine the radiative emission rate and the quantum efficiency of PbS quantum dots, inspired by experiments performed by Drexhage [55, 56]. Information on these physical properties is crucial if one wishes to interpret QED emission experiments from ab-initio. Typically, colloidal quantum dots have a quantum efficiency of 30 to 80% [57]. The quantum efficiency may change if the quantum dots are placed in a different environment, as different environments may entail different non-radiative and radiative decay rates [45].

In sec. 2.2 it was mentioned that the quantum efficiency is defined as $\eta \equiv \frac{\gamma_{\mathrm{rad}}^{\mathrm{hom}}}{\gamma}$, where $\gamma = \gamma_{\mathrm{rad}}^{\mathrm{hom}} + \gamma_{\mathrm{non,rad}}$. We determine the quantum efficiency by measuring the total decay rate $\gamma$ for different normalized LDOS. According to Fermi's Golden Rule, the radiative decay rate $\gamma_{\mathrm{rad}}$ increases linearly with the LDOS $\rho$. The non-radiative decay rate $\gamma_{\mathrm{non,rad}}$ should remain independent of the LDOS. By measuring the total decay rate $\gamma$ as a function of the LDOS, one can both determine $\gamma_{\mathrm{rad}}^{\mathrm{hom}}$ and $\gamma_{\mathrm{non,rad}}$, from which $\eta$ can be obtained.

PbS quantum dots have been placed close to planar interfaces to control the LDOS. Let us consider the situation when an emitter radiates an electromagnetic field and that the field is reflected on the interface. The reflected field interferes with the electric field of the emitter. If the reflected field is in phase, the LDOS at the emitter site will be increased, and emission will be enhanced. If the reflected field is out of phase, the LDOS decreases and emission will be inhibited [27, 55].

The types of samples used in this experiment are shown in Fig. A.1. Fig. A.1($a$) shows the situation where the quantum dots are embedded in a homogeneous medium with an LDOS equal to $\rho_{\mathrm{hom}}$. A layer of polymethyl methacrylate (495 PMMA) that contains the PbS quantum dots is spin coated with $(15 \pm 5)$ nm thickness on a glass substrate, where the thickness is determined with profilometry. Based on the concentrations of PMMA and quantum dots, there is about 1 quantum dot per 100 nm$^2$, which is a sufficiently low density to avoid non-radiative quenching effects. A thick $\sim 1$ $\mu$m layer of polyvinyl alcohol (PVA) is spin coated on top of the PMMA layer containing the quantum dots. For visible wavelengths, PMMA has a refractive index of $n_{\mathrm{PMMA}} = 1.49 \pm 0.01$ and PVA has $n_{\mathrm{PVA}} = 1.50 \pm 0.01$ [56]. The approximation is made that every layer has the same

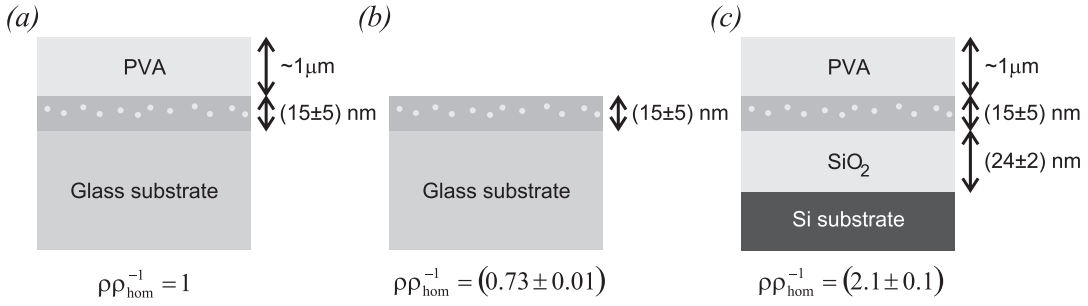


**Figure A.1:** Schematic cross sections of three types of samples used in the measurements.

refractive index of $n = 1.49$ for an emission wavelength of 1500 nm. The normalized isotropic LDOS inside the quantum dot layer is set at $\rho\rho_{hom}^{-1} = 1$.

Fig. A.1($b$) shows the situation of an emitter close to a reflecting surface. This situation can be modeled as an emitter close to a planar interface between 0 and 15 nm , where the quantum dots are embedded in a layer with $n = 1.49$. The calculated normalized isotropic LDOS is $\rho\rho_{hom}^{-1} = 0.73 \pm 0.01$. The calculations are based on the models described in [27, 58].

Fig. A.1($c$) shows the emitters inside a medium with $n = 1.49$, placed about 30 nm away from a silicon layer with $n = 3.5$. It is assumed that $SiO_2$ ($n_{SiO_2} 1.4 \pm 0.1$ at a wavelength of 1500 nm, determined by ellipsometry), PMMA and PVA have the same refractive index of 1.49. The thickness of the $SiO_2$ layer is determined by ellipsometry. The normalized isotropic LDOS inside the PMMA layer is $\rho\rho_{hom}^{-1} = 2.1 \pm 0.1$.

The samples were placed in a nitrogen chamber to prevent photo-oxidation. The spin coated quantum dots remained stable for approximately one day. The quantum dots were excited with a frequency doubled $Nd^{3+}$:Yag laser (Time-Bandwidth, Cougar) with an emission wavelength of 532 nm, repetition rate of 409 kHz and a pulse width of 11 ps[1]. The emission was collected at a wavelength of 1500 nm. The decay curves have been fitted with a lognormal distribution of the decay rates [36] to obtain the most frequent decay rate. The most frequent decay rate is used to calculate the quantum efficiency.

Examples of measured decay curves are shown in Fig. A.2. The curves were fitted between 0 (time directly after excitation of the quantum dots) and 500 ns. For the homogeneous situation ($a$), the decay curve does not agree well with a single-exponential decay rate, since the goodness of the fit strongly differs from one: $\chi^2_{red} = 6.55$. This is likely caused by the low signal level compared to the background counts; between 0 and 300 ns, a clear decay is visible and the single-exponential decay seems to fit the collected data, but mainly background counts dominate between 300 and 500 ns, which are not well modeled. For the situation when the quantum dots are placed close to a reflecting interface ($b$), a non-exponential decay is observed. This agrees with the expectation that the quantum dots decay with different rates because of different orientations and positions relative to the reflecting interface.

An overview of the most frequent decay rates on the three kinds of samples is presented in Fig. A.3. Each decay curve was collected in approximately 1 hour to obtain sufficient count statistics. Each point corresponds with a different location on a sample. Each fit has a goodness varying between $0.75 < \chi^2_{red} < 1.35$, demonstrating that the fitted decay curves are in good agreement with measured decay curves.

[1] Excitation path 1 was used in Fig. 3.7

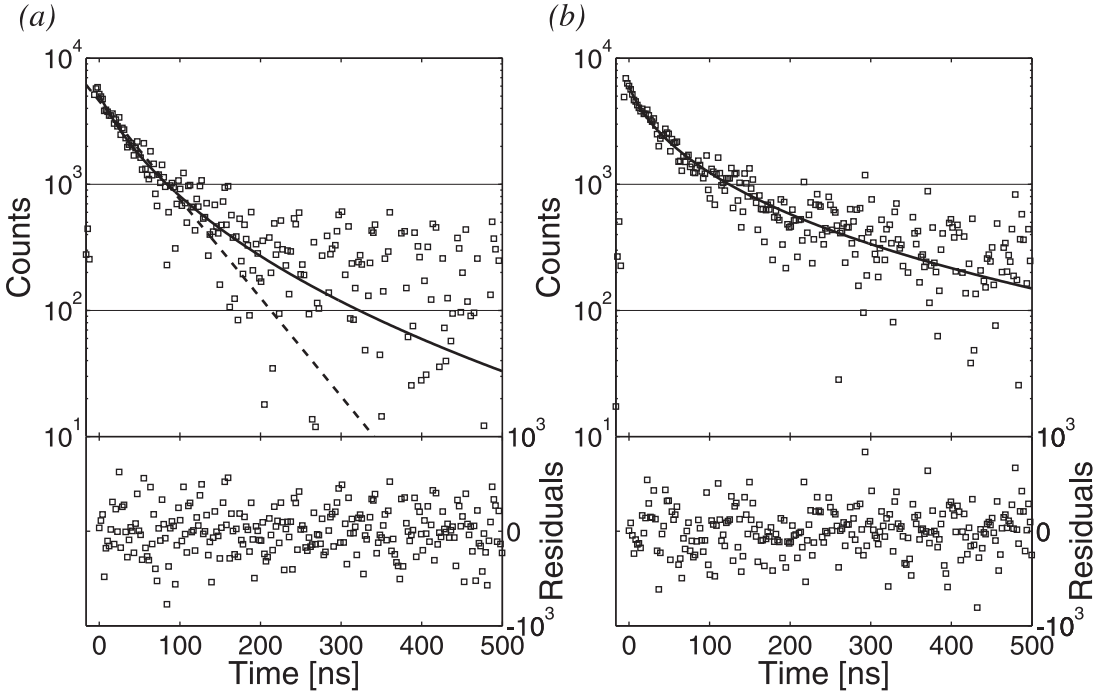


**Figure A.2:** (*a*) Decay curve obtained for a sample like Fig. A.1(*a*). The dashed line is a single-exponential fit of the decay with a goodness of $\chi^2_{red} = 6.55$. The solid line is a fit based on a lognormal distribution of the decay rates with a goodness of $\chi^2_{red} = 0.95$. The residuals of this fit are shown in the bottom panel. This decay curve corresponds with measurement 17 in Fig. A.3. (*b*) Decay curve obtained for a sample like Fig. A.1(*b*). The solid line is a fit based on a lognormal distribution of the decay rates with a goodness of $\chi^2_{red} = 1.04$. The residuals of this fit are shown in the bottom panel. This decay curve corresponds with measurement 6 in Fig. A.3. Both decay curves have a bin size of 2.048 ns.

Measurements 1 to 12 were performed on the samples of Fig. A.1(*b*), on four different samples. Small differences are observed in the determined most frequent decay rate between each sample individually. For especially the second and third sample, the most frequent decay rate is independent of the measurement location on the sample, demonstrating these samples are of excellent quality. The average most frequent decay rate for this type of sample is $\gamma_{\text{av}} = (8.0 \pm 0.9) \cdot 10^{-3}$ ns$^{-1}$, where the error is given by two times the standard deviation of the average most frequent decay rate.

Measurements 13 to 18 were performed on two different samples of Fig. A.1(*a*). Small differences are observed in the most frequent decay rate between each sample individually. The average most frequent decay rate for this type of sample is given by $\gamma_{\text{av}} = (11.0 \pm 2.3) \cdot 10^{-3}$ ns$^{-1}$. The average most frequent decay rate is larger than for the previous type of sample, as expected from the increased isotropic LDOS.

Measurements 19 to 21 were performed on the samples of Fig. A.1(*c*), collected on one sample. The average most frequent decay rate for this type of sample is given by $\gamma_{\text{av}} = (8.1 \pm 1.7) \cdot 10^{-3}$ ns$^{-1}$. Surprisingly, this decay rate is lower than for the previous type of sample, although we expected the LDOS to increase by a factor two. The reason for the decreased decay rate is unknown. The reduced most frequent decay rate might be caused by changes in the non-radiative decay rate of the quantum dots. One may speculate that this is related to the fact that the substrate is different than in the other two samples. Koenderink et al. [39] mention that for low quantum efficiencies, the emitted

power is directly proportional to the radiative decay rate and hence to the LDOS. The signal counts for the samples of Fig. A.1($c$) were about 20% lower than for the samples of Fig. A.1($b$), indicating this effect is not observed.

The average decay rate for the three types of samples as a function of the calculated normalized isotropic LDOS is shown in Fig A.4. The average most frequent decay rate for the samples of Fig. A.1($b$) is clearly lower than for the samples of Fig. A.1($a$), as expected from the different LDOS. The most frequent decay rate for quantum dots spin coated on silicon is much smaller than expected. The dashed line is tentatively drawn through the average decay rates for the samples with a glass substrate. This line would give a non-radiative decay rate of $\gamma_{\text{non,rad}} = 0.26 \cdot 10^{-3}$ ns$^{-1}$, a homogeneous radiative decay rate of $\gamma_{\text{rad}}^{\text{hom}} = 11 \cdot 10^{-3}$ ns$^{-1}$ and a corresponding quantum efficiency of $\eta = 98\%$. If one also considers the samples with silicon substrate, one gets the horizontal dash-dotted line corresponding with $\eta = 0\%$. However, this hypothesis is inconsistent with the observed count rates.

We have measured fluorescence decay of PbS quantum dots in order to obtain the quantum efficiency. Three types of samples have been used to control the LDOS. The fitted most frequent decay rate, based on a lognormal distribution of the decay rates, depends on the types of samples used. We conclude that the quantum efficiency cannot be determined from the obtained data due to low signal levels. The obtained decay curves showed a decay of typically one decade before the signal became dominated by background counts.

The results might be improved by increasing the signal level by, for example, collecting decay curves over a longer time interval. We propose to embed quantum dots in similar samples as described by [56], to make sure the non-radiative decay rate remains the same for every sample. Disadvantage of this method is that one can vary the normalized LDOS between approximately $1 < \rho\rho_{hom}^{-1} < 1.8$.

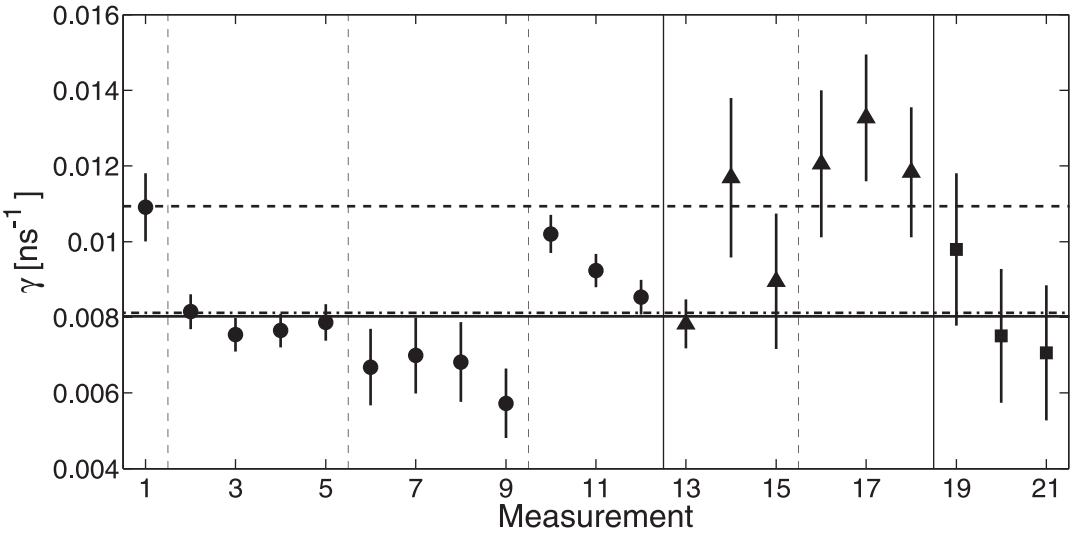


**Figure A.3:** Overview of the fitted most frequent decay rates for every measurement. Circles denote samples of Fig A.1($b$), triangles samples of Fig A.1($a$) and squares samples of Fig A.1($c$). The errors are given by two times the standard deviation of the fitted most frequent decay rate. Each measurement was taken at a different location on the sample. Vertical solid lines mark different types of samples, vertical dashed lines mark different samples of the same type. The horizontal solid line is the average most frequent decay rate for samples of Fig A.1($b$), the dashed line for samples of Fig A.1($a$) and the dash-dotted line for Fig A.1($c$).

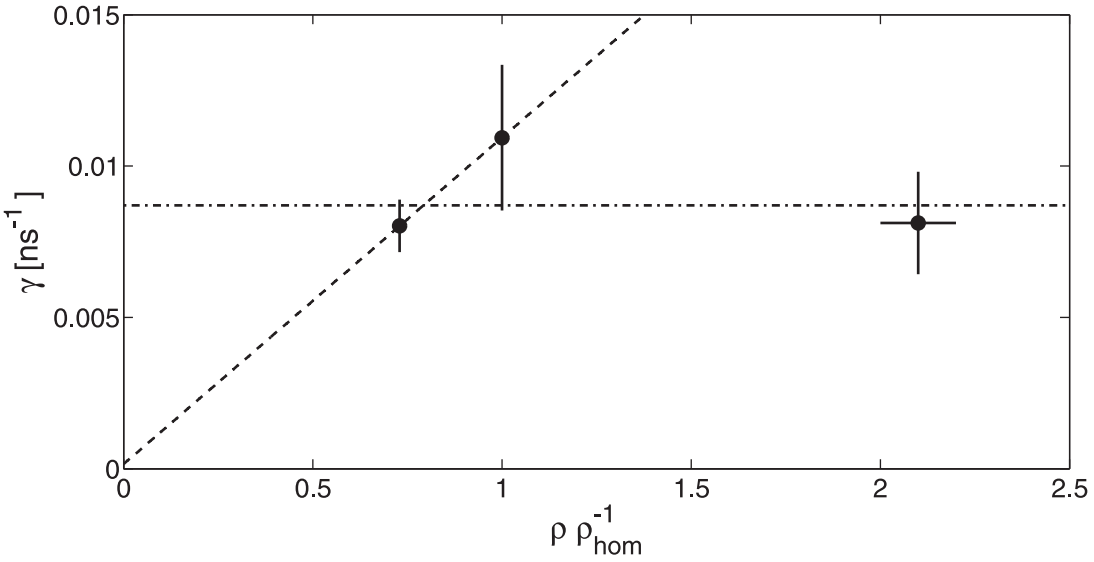


**Figure A.4:** Average most frequent decay rate for the types of samples of Fig. A.1 as a function of the calculated normalized isotropic LDOS. The dashed line is a linear best fit of the average decay rates corresponding to the samples with a glass substrate. The horizontal dash dotted line is drawn through all data, indicating zero quantum efficiency.

# Bibliography


[1] E. Yablonovitch. Inhibited spontaneous emission in solid-state physics and electronics. *Physical Review Letters*, 58:2059–2062, 1987.

[2] J.D. Joannopoulos, S.G. Johnson, J.N. Winn, and R.D. Meade. *Photonic Crystals Molding the Flow of Light*. Princeton University Press, second edition, 2008.

[3] N.W. Ashcroft and N.D. Mermin. *Solid state physics*. Thomson Learning, 1976.

[4] J.D. Joannopoulos, P.R. Villeneuve, and S. Fan. Photonic crystals: putting a new twist on light. *Nature*, 386:143–149, 1997.

[5] K.J. Vahala. Optical microcavities. *Nature*, 424:839–846, 2003.

[6] P. Lodahl, A.F. van Driel, I.S. Nikolaev, A. Irman, K. Overgaag, D. Vanmaekelbergh, and W.L. Vos. Controlling the dynamics of spontaneous emission from quantum dots by photonic crystals. *Nature*, 430:654–657, 2004.

[7] E.M. Purcell. Spontaneous emission probabilities at radio frequencies. *Physical Review*, 69:681, 1946.

[8] R. Sprik, B.A. van Tiggelen, and A. Lagendijk. Optical emission in periodic dielectrics. *Europhysics Letters*, 35:265–270, 1996.

[9] P. Michler, A. Kiraz, C. Becher, W.V. Schoenfeld, P.M. Petroff, L. Zhang, E. Hu, and A. Imamoglu. A quantum dot single-photon turnstile device. *Science*, 290:2282–2285, 2000.

[10] A.F. Koenderink. *Emission and Transport of Light in Photonic Crystals*. PhD thesis, University of Amsterdam, 2003.

[11] C.G. Gerry and P.K. Knight. *Introductory Quantum Optics*. Cambridge University Press, reprinted edition, 2005.

[12] L.A. Woldering, R.W. Tjerkstra, H.V. Jansen, I.D. Setija, and W.L. Vos. Periodic arrays of deep nanopores made in silicon with reactive ion etching and deep UV lithography. *Nanotechnology*, 19:145304, 2008.

[13] L.A. Woldering. *Fabrication of Photonic Crystals and Nanocavities*. PhD thesis, University of Twente, 2008.

[14] M. Ho, C.T. Chan, C.M. Soukoulis, R. Biswas, and M. Sigalas. Photonic band gaps in three dimensions: new layer-by-layer periodic structures. *Solid State Communications*, 89(5):413–416, 1994.

[15] R. Hillebrand and W. Hergert. Scaling properties of a tetragonal photonic crystal design having a large complete bandgap. *Photonics and Nanostructures - Fundamentals and Applications*, 2:33–39, 2004.

[16] L.A. Woldering, A.P. Mosk, R.W. Tjerkstra, and W.L. Vos. The influence of fabrication deviations on the photonic band gap of three-dimensional inverse woodpile nanostructures. *Journal of Applied Physics*, 105:093108, 2009.

[17] A. Hartsuiker. *Ultrafast all-optical switching and optical properties of microcavities and photonic crystals*. PhD thesis, University of Twente, 2009.

[18] W.L. Bragg. The diffraction of short electromagnetic waves by a crystal. *Proceedings of the Cambridge Philosophical Society*, 17:43–57, 1913.

[19] A. Yariv and P. Yeh. *Optical Waves in Crystals*. John Wiley & Sons, 1984.

[20] W.L. Vos, H.M. van Driel, M. Megens, A.F. Koenderink, and A. Imhof. Experimental probes of the optical properties of photonic crystals. In C.M. Soukoulis, editor, *Proceedings of the NATO ASI "Photonic Crystals and Light Localization in the 21st century"*, pages 181–198, 2001.

[21] W.L. Vos, R. Sprik, A. van Blaaderen, A. Imhof, A. Lagendijk, and G.H. Wegdam. Strong effects of photonic band structures on the diffraction of colloidal crystals. *Physical Review B*, 53:16231–16235, 1996.

[22] W. Friedrich, P. Knipping, and M. Laue. *Sitzungsberichte der Königlich Bayerischen Akademie der Wissenschaften*, 303, 1912.

[23] H. Ibach and H. Lüth. *Solid-state physics; an introduction to principles of materials science*. Springer, 2003.

[24] H.M. van Driel and W.L. Vos. Multiple Bragg wave coupling in photonic band-gap crystals. *Physical Review B*, 62:9872–9875, 2000.

[25] W.L. Vos and H.M. van Driel. Higher order Bragg diffraction by strongly photonic fcc crystals: onset of a photonic bandgap. *Physics Letters A*, 272:101–106, 2000.

[26] K. Sakoda. Symmetry, degeneracy, and uncoupled modes in two-dimensional photonic lattices. *Physical Review B*, 52:7982–7986, 1995.

[27] W.L Barnes. Fluorescence near interfaces: the role of photonic mode density. *Journal of Modern Optics*, 45:661–699, 1998.

[28] I.S. Nikolaev. *Spontaneous-emission rates of quantum dots and dyes controlled with photonic crystals*. PhD thesis, University of Twente, 2006.

[29] E. Fermi. Quantum theory of radiation. *Review of Modern Physics*, 4:87–132, 1932.

[30] J.S. Kole. *New Methods for the Numerical Solution of Maxwell's Equations*. PhD thesis, University of Groningen, 2003.

[31] K. Ishizaki, M. Okano, and S. Noda. Numerical investigation of emission in finite-sized three-dimensional photonic crystals with structure fluctuations. *Journal of the Optical Society of America B*, 26:1157–1161, 2009.

[32] W.L. Vos. Private communication.

[33] M. Fujita, S. Takahashi, Y. Tanaka, T. Asano, and S. Noda. Simultaneous inhibition and redistribution of spontaneous light emission in photonic crystals. *Science*, 308:1296–1298, 2005.

[34] B. Julsgaard, J. Johansen, S. Stobbe, T. Stolberg-Rohr, T. Sunner, M. Kamp, A. Forchel, and P. Lodahl. Decay dynamics of quantum dots influenced by the local density of optical states of two-dimensional photonic crystal membranes. *Applied Physics Letters*, 93:094102–1–3, 2008.

[35] I.S. Nikolaev, W.L. Vos, and A.F. Koenderink. Accurate calculation of the local density of optical states in inverse-opal photonic crystals. *Journal of the Optical Society of America B*, 26:987–997, 2009.

[36] A.F. van Driel, I.S. Nikolaev, P. Vergeer, P. Lodahl, D. Vanmaekelbergh, and W.L. Vos. Statistical analysis of time-resolved emission from ensembles of semiconductor quantum dots: Interpretation of exponential decay models. *Physical Review B*, 75:035329–1–8, 2007.

[37] J.R. Lakowicz. *Principles of Fluorescence Spectroscopy*. Springer, New York, third edition, 2006.

[38] I.S. Nikolaev, P. Lodahl, A.F. van Driel, A.F. Koenderink, and W.L. Vos. Strongly nonexponential time-resolved fluorescence of quantum-dot ensembles in three-dimensional photonic crystals. *Physical Review B*, 75:115302, 2007.

[39] A.F. Koenderink, L. Bechger, H.P. Schriemer, A. Lagendijk, and W.L. Vos. Broadband fivefold reduction of vacuum fluctuations probed by dyes in photonic crystals. *Physical Review Letters*, 88:143903, 2002.

[40] E. van der Pol. Addressing single optical resonances of micropillar cavities. Master's thesis, University of Twente, 2009.

[41] B.E.A. Saleh and M.C. Teich. *Fundamentals of Photonics*. Wiley-Interscience, second edition, 2007.

[42] G.R. Fowles. *Introduction to modern optics*. Dover publications, second edition, 1975.

[43] S. Rowson, A. Chelnokov, C. Cuisin, and J. M. Lourtioz. Three-dimensional characterization of a two-dimensional photonic bandgap reflector at midinfrared wavelengths. In IEE Proceedings-Optoelectron., editor, *Photonic Crystals and Microstructures*, volume 145, pages 403–408, 1998.

[44] S. Rowson, A. Chelnokov, C. Cuisin, and J. M. Lourtioz. Two-dimensional photonic bandgap reflectors for free-propagating beams in the mid-infrared. *Journal of Optics A: Pure and Applied Optics*, 1:483–489, 1999.

[45] B.H. Husken. *Spontaneous emission of near-infrared quantum dots controlled with photonic crystals*. PhD thesis, University of Twente, 2009.

[46] J. Schilling, A. Birner, F. Müller, R. B. Wehrspohn, R. Hillebrand, U. Gösele, K. Busch, S. John, S. W. Leonard, and H. M. van Driel. Optical characterization of 2d macroporous silicon photonic crystals with bandgaps around 3.5 and 1.5 $\mu$m. *Optical Materials*, 17:7–10, 2001.

[47] V.N. Astratov, I.S. Culshaw, R.M. Stevenson, D.M. Whittaker, M.S. Skolnick, T.F. Krauss, and R.M. De La Rue. Resonant coupling of near-infrared radiation to photonic band structure waveguides. *Journal of Lightwave Technology*, 17:2050–2057, 1999.

[48] V.N. Astratov, D.M. Whittaker, I.S. Culshaw, R.M. Stevenson, M.S. Skolnick, T.F. Krauss, and R.M. De La Rue. Photonic band-structure effects in the reflectivity of periodically patterned waveguides. *Physical Review B*, 60:16255–16258, 1999.

[49] N. Paraire and Y. Benachour. Investigation of planar photonic crystal band diagrams under the light cone using surface coupling techniques. *Applied Physics B*, 89:245–250, 2007.

[50] K. Ishizaki and S. Noda. Manipulation of photons at the surface of three-dimensional photonic crystals. *Nature*, 460:367–370, 2009.

[51] J. Schilling, J. White, A. Scherer, G. Stupian, R. Hillebrand, and U. Gösele. Three-dimensional macroporous silicon photonic crystal with large photonic band gap. *Applied Physics Letters*, 86:011101, 2005.

[52] F.G. Santamaria, M. Xu, V. Lousse, S. Fan, P. V. Braun, and J.A. Lewis. A germanium inverse woodpile structure with a large photonic band gap. *Advanced Materials*, 19:1567–1570, 2007.

[53] A. Hermatschweiler, A. Ledermann, G.A. Ozin, M. Wegener, and G. von Freymann. Fabrication of silicon inverse woodpile photonic crystals. *Advanced Functional Materials*, 17:2273–2277, 2007.

[54] P. Kristensen, A.F. Koenderink, P. Lodahl, B. Tromborg, and J. Mork. Fractional decay of quantum dots in real photonic crystals. *Optics letters*, 33:1557–1559, 2008.

[55] K.H. Drexhage. Influence of a dielectric interface on fluorescence decay time. *Journal of Luminescence*, 1,2:693–701, 1970.

[56] M.D. Leistikow, J. Johansen, A.J. Kettelarij, P. Lodahl, , and W.L. Vos. Size dependent oscillator strength and quantum efficiency of cdse quantum dots determined by controlling the local density of states. *Physical Review B*, 79:045301, 2009.

[57] E.H. Sargent. Infrared quantum dots. *Advanced Materials*, 17:515–522, 2005.

[58] R.R. Chance, A. Prock, and R. Silbey. *Molecular fluorescence and energy transfer near interfaces*. John Wiley & Sons, 1978.